# Evaluation of radiation scheme performance within chemistry climate models

Piers M. Forster,[1] Victor I. Fomichev,[2] Eugene Rozanov,[3,4] Chiara Cagnazzo,[5] Andreas I. Jonsson,[6] Ulrike Langematz,[7] Boris Fomin,[8] Michael J. Iacono,[9] Bernhard Mayer,[10] Eli Mlawer,[9] Gunnar Myhre,[11] Robert W. Portmann,[12] Hideharu Akiyoshi,[13] Victoria Falaleeva,[14] Nathan Gillett,[15] Alexey Karpechko,[16] Jiangnan Li,[15] Perrine Lemennais,[17] Olaf Morgenstern,[18] Sophie Oberländer,[7] Michael Sigmond,[6] and Kiyotaka Shibata[19]

Received 19 November 2010; revised 25 February 2011; accepted 4 March 2011; published 18 May 2011.

[1] This paper evaluates global mean radiatively important properties of chemistry climate models (CCMs). We evaluate stratospheric temperatures and their 1980–2000 trends, January clear sky irradiances, heating rates, and greenhouse gas radiative forcings from an offline comparison of CCM radiation codes with line-by-line models, and CCMs' representation of the solar cycle. CCM global mean temperatures and their change can give an indication of errors in radiative transfer codes and/or atmospheric composition. Biases in the global temperature climatology are generally small, although five out of 18 CCMs show biases in their climatology that likely indicate problems with their radiative transfer codes. Temperature trends also generally agree well with observations, although one model shows significant discrepancies that appear to be due to radiation errors. Heating rates and estimated temperature changes from $CO_2$, ozone, and water vapor changes are generally well modeled. Other gases ($N_2O$, $CH_4$, and CFCs) have only played a minor role in stratospheric temperature change, but their heating rates have large fractional errors in many models. Models that do not account for variations in the spectrum of solar irradiance cannot properly simulate solar-induced variations in stratospheric temperature. The combined long-lived greenhouse gas global annual mean instantaneous net radiative forcing at the tropopause is within 30% of line-by-line models for all CCM radiation codes tested. Problems remain in simulating radiative forcing for stratospheric water vapor and ozone changes with errors between 3% and 200% compared to line by line models. The paper makes recommendations for CCM radiation code developers and future intercomparisons.

**Citation:** Forster, P. M., et al. (2011), Evaluation of radiation scheme performance within chemistry climate models, *J. Geophys. Res.*, *116*, D10302, doi:10.1029/2010JD015361.

[1]School of Earth and Environment, University of Leeds, Leeds, UK.
[2]ESSE, York University, Toronto, Ontario, Canada.
[3]Physikalisch-Meteorologisches Observatorium Davos/World Radiation Center, Davos, Switzerland.
[4]Institute for Atmospheric and Climate Science, ETH, Zurich, Switzerland.
[5]Centro Euro-Mediterraneo per i Cambiamenti Climatici, Bologna, Italy.
[6]Atmospheric Physics Group, Department of Physics, University of Toronto, Toronto, Ontario, Canada.
[7]Institut für Meteorologie, Freie Universität Berlin, Berlin, Germany.
[8]Central Aerological Observatory, Moscow, Russia.
[9]Atmospheric and Environmental Research, Ltd., Lexington, Massachusetts, USA.
[10]Lehrstuhl fuer Experimentelle Meteorologie, Ludwig-Maximilians-Universität, Munich, Germany.
[11]Center for International Climate and Environmental Research–Oslo, Oslo, Norway.
[12]Chemical Sciences Division, Earth System Research Laboratory, National Oceanic and Atmospheric Administration, Boulder, Colorado, USA.
[13]National Institute for Environmental Studies, Tsukuba, Japan.
[14]A.M. Obukhov Institute of Atmospheric Physics, Russian Academy of Sciences, Moscow, Russia.
[15]Canadian Centre for Climate Modelling and Analysis, University of Victoria, Victoria, British Columbia, Canada.
[16]Arctic Research Centre, Finnish Meteorological Institute, Helsinki, Finland.
[17]Service d'Aeronomie du CNRS, Paris, France.
[18]National Institute of Water and Atmospheric Research, Lauder, New Zealand.
[19]Meteorological Research Institute, Tsukuba, Japan.


0148-0227/11/2010JD015361

## 1. Introduction

[2] Understanding and quantifying radiative processes is of fundamental importance to the study of climate and its change. Radiative processes drive global climate change and play a key role in establishing the temperature structure of the atmosphere. The thermal regime of the middle atmosphere is determined to a great extent by the balance between the incoming solar and outgoing infrared radiation. The radiative heating changes brought on by changes in carbon dioxide and ozone can cause large trends in stratospheric temperatures as well as affect surface climate [e.g., *World Meteorological Organization*, 2003]. Given the prime importance of radiative processes for understanding the atmosphere and its evolution, the development and improvement of radiation schemes is obviously one of the crucial points in the ongoing development and maintenance of atmospheric models. The purpose of this paper is to evaluate key radiative processes in models participating in the SPARC Chemistry-Climate Model Validation Activity CCMVal, SPARC CCMVal (2010). The description of all participated CCMs and performed experiments was presented by *Morgenstern et al.* [2010].

[3] This paper covers a number of topics. Current radiative parameterization architecture is assessed in section 2. Global mean temperature profiles and long-term trends provided by CCMVal models are analyzed in section 3. This tests their global radiative properties. In section 4, radiative transfer schemes of different CCMVal models are compared with each other and compared against line-by-line (LBL) calculations. LBL calculations give our current best estimate to solutions of radiative transfer within the atmosphere. The incoming solar irradiance at short wavelengths significantly varies with the solar cycle, leading to strong ozone and temperature solar signals in the stratospheric climate. The ability of CCMval models' radiation schemes to reproduce the solar signal is analyzed in section 5. Section 6 presents a summary and conclusions.

[4] Table 1 presents the details of the radiative diagnostics and the metrics used to assess them. Note that throughout the paper we have tried to explain differences between CCMs employing the available diagnostics. However, in many instances appropriate diagnostics were not available and thus precise interpretation of CCM radiation biases has not been possible.

[5] Several radiative processes are not assessed in this paper. A representation of photolysis is of fundamental importance for CCMs. Above 70 km local thermodynamic equilibrium (LTE) begins to breakdown (see *Fomichev* [2009] for a detailed review of non-LTE effects). At present only two CCMs include these effects (CMAM and WACCM), and both employ the same parameterization [*Fomichev et al.*, 1998; *Ogibalov and Fomichev*, 2003]. Clouds and aerosol (both stratospheric and tropospheric) also have important effects on stratospheric heating rates and on radiative forcing but these effects are not evaluated here. We also do not assess the effects of the plane parallel atmosphere approximation that is typically employed in radiation codes. This approximation fails to give any solar heating at zenith angles larger than 90°. Last we do not assess the way the radiation scheme is implemented within the CCM. Important considerations here are the frequency

**Table 1.** Summary of the Radiative Diagnostics and the Metrics Used to Assess Them

| Process | Diagnostic | Variables | Reference Data | Metric | Section |
|---|---|---|---|---|---|
| Stratospheric temperatures | Comparing 1980–1999 climatological global mean temperature profiles | Temperature, Atmospheric composition | (Re)analyses | Maximum difference between ERA 40 and either UKMO or NCEP analysis | 3 |
| Stratospheric temperature change | Comparing 1980–1999 global mean temperature trends | Temperature, Atmospheric composition | MSU/SSU trends | MSU/SSU trend uncertainty 95% confidence interval | 3 |
| Radiative fluxes | Comparing climatological fluxes in offline radiation schemes | Shortwave, longwave up/down/net fluxes for global daily average | Line-by-line and other sophisticated offline radiation models | Maximum difference between sophisticated radiation models | 4 |
| Radiative forcing | Comparing forcings in offline radiation schemes for a variety of atmospheric composition changes | Global and diurnal mean shortwave, longwave up/down/net instantaneous forcings. | Line-by-line and other sophisticated offline radiation models | Maximum difference between sophisticated radiation models | 4 |
| Stratospheric heating/cooling | Comparing climatological heating/cooling rates in offline radiation schemes | Global and diurnal mean shortwave, longwave/net heating rates | Line-by-line and other sophisticated offline radiation models | Maximum difference between sophisticated radiation models | 4 |
| Changes in stratospheric heating/cooling | Comparing changes in heating/cooling rates in offline radiation schemes | Global and diurnal mean changes in shortwave, longwave, net heating rates | Line-by-line and other sophisticated offline radiation models | Maximum difference between sophisticated radiation models | 4 |
| Solar variability | Comparing SW heating rates in offline radiation schemes with prescribed solar spectrum variations and ozone change | Shortwave heating rates | Sophisticated offline radiation model | Whether or not radiation code reproduces sophisticated model signal | 5 |

of full radiative calculations compared to the model time step; sub-grid-scale variations and the order of the radiation call in relation to the call to other physical parameterizations.

## 2. Radiative Transfer Parameterizations

[6] Accurate methods of solving radiative transfer within the Earth's atmosphere exist. However, such schemes are too computationally expensive to currently be employed within a climate modeling context. Parameterizations were designed to approximate more exact treatments with sufficient enough accuracy for the problem being considered. A good example of this is one of the earliest parameterizations of solar radiative transfer [*Lacis and Hansen*, 1974]. Their approximations provide useful insights into more complex ones used today. Even their simple parameterization accounted for Rayleigh scattering, cloud, solar zenith angle, water vapor and ozone absorption, but like many shortwave codes today it ignored minor absorption by $CO_2$ and $CH_4$ [see *Collins et al.*, 2006]. For its purpose the code was extremely accurate and only increased the computer time overhead in the parent model by 0.3%; variants of this code were employed in climate models until very recently. Much of their original paper was concerned with finding measurements of input properties to test their code and they made the point that uncertainties in water vapor or cloud radiative properties are likely to be a bigger source of error than their approximate radiative transfer solution; this still remains true today.

[7] Radiative transfer approximations within climate models encompass three broad categories of (1) radiative transfer solution, (2) input parameters and (3) implementation. These are described briefly below.

[8] 1. The most important choice of the radiative transfer solution approach is the number of spectral bands to employ and how to account for overlapping within bands. Also important are the number of streams used for scattering approximations. In the CCM context it is also worth considering the choice of a plane parallel atmosphere: nearly all climate models including CCMs adopt this approximation, even when the photolysis codes in CCMs adopt spherical geometry. Most CCMs would therefore not have any solar heating at zenith angles greater than 90°, but still have photolysis of ozone in the stratosphere, creating an inconsistency.

[9] 2. Important choices of input parameters include line databases and cross sections for the absorbing gases and the water vapor continuum; the extraterrestrial solar spectrum; and cloud and aerosol optical properties.

[10] 3. CCMs and climate models also have to make pragmatic choices about how often to call the radiative transfer code, as calling the code every time step is often impractical and unnecessary. Also, choices of cloud overlap and sub-grid-scale variability need to be made. Ways of calculating solar zenith angle and Earth-Sun distance can also cause differences between models. Differences in the underlying model's vertical resolution can also affect the radiation scheme.

[11] Several previous intercomparisons of climate model radiative transfer codes have been undertaken [e.g., *Forster et al.*, 2001; *Collins et al.*, 2006; *Goldblatt et al.*, 2009; *Myhre et al.*, 2009]. Most of these studies have found very significant differences between radiation codes, even when considering only clear skies and constraining many of the input parameters. Common problems identified have been the use of radiation codes beyond their original limitations and/or using outdated input data for, for example, spectral line databases.

[12] Some details of the CCM radiation codes employed are presented in Tables 2a and 2b. All employ versions of the two stream approximation for solving scattering and have an order of 10 spectral bands in the shortwave and longwave. Although all codes include the main absorbers, minor absorbers differ between codes. They also employ different spectral line databases.

## 3. Global Mean Temperature and Temperature Trends in CCMs

[13] In this section the performance of the models in terms of their global mean temperature climatology and global mean temperature trends is assessed. On a globally averaged basis the temperature in the middle atmosphere below about 70 km is controlled mainly by radiative processes [e.g., *Fels*, 1985; *Fomichev and Shved*, 1994]. This means that long-term global mean temperature biases between models and observations are mainly due to either inaccuracies in the model treatments of radiative processes or due to inaccurate distributions of radiatively active gases in the models. Below 70 km the major contributions to the radiative energy budget are provided by ozone, carbon dioxide, and water vapor [*London*, 1980; *Brasseur and Solomon*, 2005]. For CCMVal, carbon dioxide is specified identically in all models so its abundance should not contribute to any model differences. However, the distributions of ozone and water vapor, which are affected by the transport and chemistry schemes of each individual model, affect the calculated temperature biases. Overestimation of ozone should generally lead to a warm bias (due to larger ozone solar heating) while overestimation of water vapor should generally lead to a cold bias (due to larger infrared cooling), and vice versa. Thus, intercomparison of model results for temperature on the one hand and ozone and water vapor on the other hand provides some guidance as to whether model temperature biases are due to biases in the abundance of these chemical species or due to inaccuracies in the radiation schemes.

[14] A model's ability to reproduce the observed temperature climate does not ensure an accurate sensitivity to perturbations, such as increasing GHGs and ozone depletion. Therefore we assess model temperatures and model temperature trends separately. The model temperature climatologies are discussed in section 3.1 and the model temperature trends for the past and future are discussed in sections 3.2 and 3.3, respectively.

[15] The analyses presented for the climatology and the past trends are based on model results from the CCMVal REF-B1 scenario, including observed surface forcings of sea surface temperatures (SSTs), greenhouse gases (GHGs) and ozone depleting substances (ODSs), and variations in volcanic aerosols and solar forcing. To asses future trends, however, model results for the CCMVal REF-B2 scenario are used. The REF-B2 experiments include the same surface forcing of GHGs and ODSs as REF-B1 but do not include

**Table 2a.** Shortwave Radiation Scheme Characteristics[a]

| CCM | Reference | Description | Clouds | Spectral Interval Boundaries (nm) | Absorbing Gases |
|---|---|---|---|---|---|
| CAM3.5 | *Briegleb* [1992]; *Collins et al.* [2004] | Δ-Eddington 2-s | Random/maximum overlap | 19 intervals (>200 nm); <200 nm consistent with photolysis. | $O_2$, $O_3$, $CO_2$, $H_2O$ |
| CCSRNIES | *Nakajima and Tanaka* [1986]; *Nakajima et al.* [2000] | 2-s | Random overlap | [200,217], [217,233], [233,278], [278,290], [290,303], [303,317], [317,690], [690,2500], [2500,4000] | $O_2$, $O_3$, $CO_2$, $H_2O$ |
| CMAM | *Fouquart and Bonnel* [1980]; *Fomichev et al.* [2004] | Δ 2-s | Maximum or random overlap | [250,690], [690,1190], [1190,2380], [2380,4000]; Separate parameterizations for near-IR $CO_2$ [1200,4300] above 1 hPa and $O_2$ absorption in SRC [125–175] and SRB [175–205] above 0.25 hPa | $O_2$, $O_3$, $CO_2$, $H_2O$ |
| CNRM-ACM | *Morcrette* [1990, 1991] | Fourquart-Morcrette 2-s | Maximum random overlap | [250,680], [680,4000] | $O_3$, $H_2O$, $O_2$, $CO_2$, $CH_4$, $N_2O$ |
| E39CA | *Fouquart and Bonnel* [1980] | Δ 2-s | Maximum to random overlap | [245–685] | $O_2$, $O_3$, $CO_2$, $H_2O$ |
| EMAC | *Nissen et al.* [2007]; *Fouquart and Bonnel* [1980]; *Roeckner et al.* [2003] | Δ 2-s | Maximum to random overlap | [121.6], [125,175], [175,205], [206,244], [244,278], [278,362], [362,683] (49 bands), [690,1190], [1190,2380], [2380,4000] | $O_2$, $O_3$, $CO_2$, $H_2O$ |
| GEOSCCM | *Chou and Suarez* [1999]; *Sud et al.* [1993]; *Chou et al.* [1998] | Δ-Eddington2-s | Maximum random overlap | [175–225], [225–245], [245–260], [280–295], [295–310], [310–320], [320–400], [400–700], [700–1220], [1220–2270], [2270–10000] | $O_2$, $O_3$, $CO_2$, $H_2O$ |
| LMDZrepro | *Fouquart and Bonnel* [1980] | 2.s | Maximum or random overlap | [250,680], [680,4000] | $O_2$, $O_3$, $CO_2$, $H_2O$ |
| MRI | *Briegleb* [1992]; *Shibata and Uchiyama* [1994] | Δ 2-s. DOM | Maximum to random overlap | [200,245], [245,265], [265,275], [275,285], [285,295], [295,305], [205,350], [350,700], [700,5000], [2630–2860], [4160–4550] | $O_2$, $O_3$, $CO_2$, $H_2O$ |
| Niwa-SOCOL SOCOL | *Fouquart and Bonnel* [1980]; *Egorova et al.* [2004] | Δ 2-s | Maximum or random overlap | [250–680], [680–4000]; parameterization for $O_2$ and $O_3$ absorption in L-$\alpha$ [121–122], SRB [175–205] and HC [200–250] | $O_2$, $O_3$, $CO_2$, $H_2O$ |
| ULAQ | *Lacis et al.* [1992]; *Pitari* [1993]; *Pitari et al.* [2002] | Δ-Eddington 2-s | Maximum random overlap | 21 intervals [135, 175]; 14 intervals [175, 200]; 19 intervals [200, 245]; 19 intervals [245, 320]; 11 intervals [320, 690]; 16 intervals [690, 10000] | $O_2$, $O_3$, $CO_2$, $H_2O$, $NO_2$ |
| UMETRAC UMSLIMCAT | *Edwards and Slingo* [1996]; *Zdunkowski et al.* [1980]; *Zhong et al.* [2001] | 2-s. | Maximum to random overlap | [116,175], [175,200], [200,245], [245,320], [320,690], [320,690], [690,1190], [1190,2380], [2380,10000] | $O_2$, $O_3$, $CO_2$, $H_2O$ |
| UMUKCA-METO UMUKCA-UCAM | *Edwards and Slingo* [1996]; *Zdunkowski et al.* [1980]; *Zhong et al.* [2008] | 2-s. | Maximum to random overlap | [200,320], [320,690], [320,690], [690,1190], [1190,2380], [2380,10000] | $O_2$, $O_3$, $CO_2$, $H_2O$ |
| WACCM | *Briegleb* [1992]; *Collins et al.* [2004] | Δ-Eddington 2-s | Random/maximum overlap | 19 intervals (>200 nm); <200 nm consistent with photolysis. | $O_2$, $O_3$, $CO_2$, $H_2O$ |

[a]Abbreviation 2-s denotes two-stream.

**Table 2b.** Longwave Radiation Scheme Characteristics[a]

| CCM | Reference | Description | Spectral Interval Boundaries ($\mu$m) | Absorbing Gases | Chemical Heating | Non-LTE |
|---|---|---|---|---|---|---|
| CAM3.5 | *Collins et al.* [2004] | Broad band approach | *Collins et al.* [2004] | $H_2O$, $CO_2$, $O_3$, $CH_4$, $N_2O$, F11, F12, NO | No | No |
| CCSRNIES | *Nakajima et al.* [2000] | Discrete ordinate and k-distribution | [4.00,5.00], [5.00,7.14], [7.14,9.09], [9.09,10.1], [10.1,13.0], [13.0,18.2], [18.2,25.0], [25.0,40.0], [40.0,200] | $H_2O$, $CO_2$, $O_3$, $CH_4$, $N_2O$, CFCs | No | No |
| CMAM | *Morcrette* [1991]; *Fomichev et al.* [2004] | >39 hPa: 2-s; <6.7 hPa: Matrix parameterization 6.7–39: Merging region | Below 39 hPa: [6.9,8.0: 3.5,5.3], [9.0,10.3], [10.3,12.5: 8.0,9.0], [12.5,20.0], [20.0,28.6], [28.6,10000: 5.3,6.9]; Above 6.7 hPa: 15 $\mu$m $CO_2$, 9.6 $\mu$m $O_3$ and rotational $H_2O$ bands | Below 39 hPa: $H_2O$, $CO_2$, $O_3$,, $CH_4$, $N_2O$, F11, F12; Above 6.7 hPa: $H_2O$, $CO_2$, $O_3$ | Yes | Yes ($CO_2$, $O_3$, $O_2$) |
| CNRM-ACM | *Morcrette* [1990, 1991] | FMR; 2-stream | [28.6,-] + [5.3,6.9], [20.0,28.6], [12.5,20], [10.3,12.5] + [8,9], [9,10.3], [6.9,8] + [3.5,5.3] | $O_3$, $H_2O$, $CO_2$, $CH_4$, $N_2O$, F11 | No | No |
| E39CA | *Morcrette* [1991] | Broadband flux emissivity method in six spectral intervals | [3.55,8][8,10.31][10.31,12.5][12.5,20] [20,28.57][28.57,1000] wavenumbers 0 to $2.82 \times 10^5$ $m^{-1}$ | $H_2O$, $CO_2$, $O_3$, $CH_4$, $N_2O$, F11, F12 | No | No |
| EMAC | *Roeckner et al.* [2003]; *Mlawer et al.* [1997] | Correlated-k method, RRTM | [3.3,3.8], [3.8,4.2], [[4.2,4.4], [4.4,4.8], [4.8,5.6], [5.6,6.8], [6.8,7.2], [7.2,8.5], [8.5,9.3], [9.3,,10.2], [10.2,12.2], [12.2,14.3], [14.3,15.9], [15.9,20], [20,40], [40,1000] | $H_2O$, $CO_2$, $O_3$, $CH_4$, $N_2O$, F11, F12 | No | No |
| GEOSCCM | *Chou et al.* [2001] | k-distribution and table look-up | [29.4,10000], [18.5,29.4], [16.1,18.5], [13.9,16.1], [12.5,13.9], [10.2,12.5], [9.09,10.2], [7.25,9.09], [5.26,7.25], [3.33,5.26] | $H_2O$, $CO_2$, $O_3$, F11, F12, F22, $CH_4$, $N_2O$ | No | No |
| LMDZrepro | *Morcrette* [1991] | Broadband flux emissivity method in six spectral intervals | [3.55,8][8,10.31][10.31,12.5][12.5,20] [20,28.57][28.57,1000] wavenumbers 0 to $2.82 \times 10^5$ $m^{-1}$ | $H_2O$, $CO_2$, $O_3$, $CH_4$, $N_2O$, F11, F12 | No | No |
| MRI | *Shibata and Aoki* [1989] | Multiparameter-random model | 20-550-800-1200-2200 cm-1; [4.55,8.33], [8.33,12.5], [12.5,18.2], [18..2,50] | $H_2O$, $CO_2$, $O_3$, $CH_4$, $N_2O$ | No | No |
| Niwa-SOCOL SOCOL | *Morcrette* [1991] | Broadband approach | [6.9–8 and 3.5–5.3], [9–10.3], [10.3–12.5 and 8–9], [12.5,20], [20,28.6], [28.6,10000 and 5.3,6.9] | CH4, N2O, F11, F12, $CO_2$, $H_2O$, $O_3$ | No | No |
| ULAQ | *Andrews et al.* [1987]; *Lacis et al.* [1992]; *Pitari* [1993] | Broad Band Approach | [18.2,28.6], [12.5,18.2], [8.3,12.5], [3.3,7.5] | $H_2O$, $CO_2$, $O_3$ | No | No |
| UMETRAC UMSLIMCAT | *Edwards and Slingo* [1996]; *Zdunkowski et al.* [1980]; *Zhong and Haigh* [2001] | 2-s. | [28.6,10000], [18.2,28.6], [12.5,18.2], [13.3,16.9], [8.33,12.5], [8.93,10.1], [6.67,8.33], [8.93,10.1], [6.67,8.33], [5.26,6.67], [3.34,5.26] | $H_2O$, $CO_2$, $O_3$, $CH_4$, $N_2O$, F11, F12 | No | No |
| UMUKCA-METO UMUKCA-UCAM | *Edwards and Slingo* [1996]; *Zdunkowski et al.* [1980] | 2-s. | [25,10000], [18.2,25], [12.5,18.2], [13.3,16.9], [8.33,12.5], [8.93,10.1], [7.52,8.33], [6.67,7.52], [3.34,6.67] | $H_2O$, $CO_2$, $O_3$, $CH_4$, $N_2O$, F11(rescaled), F12 (rescaled) | No | No |
| WACCM | *Collins et al.* [2004] | Broad Band Approach | *Collins et al.* [2004] | $H_2O$, $CO_2$, $O_3$, $CH_4$, $N_2O$, F11, F12, NO | *Marsh et al.* [2007] | *Fomichev et al.* [1998]; *Kockarts* [1980] |

[a]Abbreviation 2-s denotes two-stream.

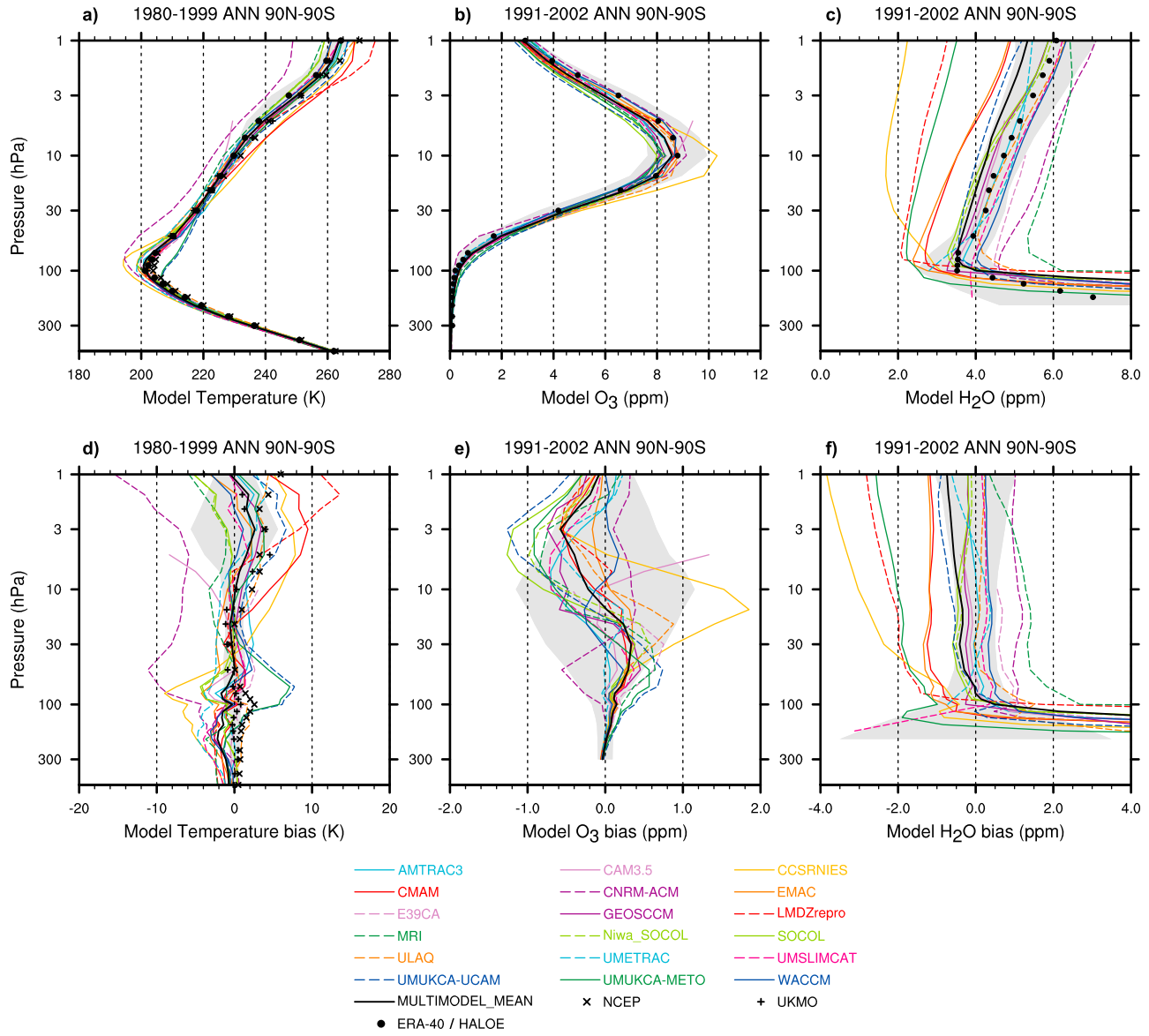


**Figure 1.** Climatological global and annual mean (a) temperature, (b) ozone mixing ratio, and (c) water vapor mixing ratio for REF-B1 model simulations and reference data sets, and (d) temperature bias, (e) ozone bias, and (f) water vapor bias with respect to reference data sets. Reference data sets include ERA-40, NCEP, and UKMO reanalyses for temperature and HALOE observations for ozone and water vapor. For temperature, the climatological means and biases are calculated for 1980–1999 except for UKMO reanalyses, which are shown for 1992–2001. Biases are calculated relative to the ERA-40 reanalyses. For ozone and water vapor, the climatological means and biases are calculated for 1991–2002 except for EMAC and UMETRAC, which are shown for 1991–2000. The gray areas show ERA-40 and HALOE ±2 standard deviations about the climatological means. The solid black lines indicate the multimodel mean results. For other data sets, see legend. Model acronyms are described in Table 1 and references therein.

variations in volcanic aerosol and solar forcing. For a complete description of the REF-B1 and REF-B2 scenarios see the *SPARC CCMVal* [2010] report. For models that have provided multiple ensemble members (for REF-B1: CMAM, CNRM-ACM, LMDZrepro, MRI, SOCOL and WACCM) the results presented show the ensemble mean values, unless stated otherwise.

### 3.1. Global Mean Temperature Climatology

[16] Figure 1a shows global mean vertical temperature profiles averaged over 1980–1999 for both the REF-B1 model experiments and for three reanalyses data sets, the latter including ERA-40, NCEP and UKMO (note that the UKMO climatology is derived for 1992–2001). The gray shaded area shows ERA-40 plus and minus two standard

deviations about the climatological mean, indicating the interannual variability of this data set. All models capture the large-scale features of the troposphere and stratosphere, with decreasing temperatures with height in the troposphere, a distinct temperature minimum at the tropopause around 100 hPa and increasing temperature with height in the stratosphere. The spread between the models is larger in the stratosphere than in the troposphere, as the tropospheric temperatures are largely controlled by the sea surface temperatures that are prescribed from observations for all models. Figure 1d shows model biases with respect to the ERA-40 climatology. NCEP and UKMO are generally close to ERA-40, but are up to 3 K warmer around the tropopause (near 100 hPa) and up to 6 K warmer in the upper stratosphere. Most models agree well with the observations and are generally within ±5 K of the ERA-40 temperatures. Exceptions are the temperatures from CAM3.5, CCSRNIES, CMAM, CNRM-ACM, LMDZrepro, UMUKCA-METO and UMUKCA-UCAM. CAM3.5, with an upper model boundary at 3 hPa, provides data only up to 5 hPa where it underestimates temperatures by up to 9 K. CCSRNIES has a cold bias around the tropopause that maximizes at −9 K near 70 hPa, and a positive bias of up to 8 K in the middle and upper stratosphere. CMAM displays a similar positive bias of up to 9 K in the middle and upper stratosphere. CNRM-ACM has a cold bias throughout the stratosphere with maximum values of −11 K and −15 K in the lower and upper stratosphere, respectively. LMDZrepro has a warm bias of up to 15 K in the upper stratosphere. UMUKCA-METO and UMUKCA-UCAM both display a distinct warm bias of up to 7–8 K in the lower stratosphere, and UMUKCA-UCAM has a warm bias of up to 6 K in the upper stratosphere. Finally it can be noted that the multimodel mean results fall within the ERA-40 interannual variability limits above about 70 hPa, i.e., throughout most of the stratosphere. Below 70 hPa, and, in particularly, in the upper troposphere between 300 and 100 hPa, there is a general tendency for the models to have a cold bias. These results are roughly in agreement with the previous multimodel temperature assessment, performed for CCMVal-1 [*Austin et al.*, 2009].

[17] Below follows a qualitative assessment that attempts to identify which features of the temperature biases highlighted above are associated with biases in ozone and water vapor. Models without a clear connection between temperature biases on the one hand, and ozone and water vapor biases on the other, are likely to have deficiencies in their radiation schemes. However, inferences drawn in this section are suggestive as our methodology cannot identify other reasons for model biases. For example, if the temperature bias were caused by a wrong prescription of the volcanic aerosols or cloud properties, our approach would attribute the bias to deficiencies in the radiation scheme. We also assume that a global relationship exists between water vapor, ozone and temperature that do not depend on local variations in the stratosphere.

[18] Figures 1b and 1c show global mean vertical ozone and water vapor profiles averaged over 1991–2002 for the REF-B1 model experiments and for HALOE observations. Figure 1e and 1f show model biases with respect to the HALOE climatology. The gray shaded areas show the HALOE plus and minus two standard deviations about the climatological mean.

[19] For ozone, model values are generally within ±1 ppm of the observations, with a tendency for the models to overestimate ozone in the lower stratosphere and to underestimate ozone in the upper stratosphere. The multimodel mean results fall well within the HALOE interannual variability limits throughout the stratosphere and upper troposphere. For water vapor the intermodel spread is much larger, and biases with respect to the observed climatology are in some cases in excess of 50% of the climatological values themselves. The multimodel mean results underestimate the observations by about 1 ppm in the stratosphere, but are within the HALOE interannual variability limits in this region. Note, unlike some climate models, stratospheric water vapor levels were not prescribed in the CCMs. Generally, ozone biases are expected to have a larger impact on the temperature than biases in water vapor, since the longwave radiative effect of water vapor generally is overshadowed by that from $CO_2$ (an exception is the lower stratosphere [see, e.g., *Fomichev*, 2009]). However, water vapor biases as large as those presented here can have a significant effect on the radiative balance throughout the stratosphere. For example, in CMAM the inclusion of water vapor cooling in the upper stratosphere leads to a temperature reduction of about 5 K in this region [*Fomichev et al.*, 2004], which suggests that large water vapor biases could have a significant impact throughout the stratosphere. Notably, all the models with a significant warm bias in the middle to upper stratosphere (CCSRNIES, CMAM and LMDZrepro) display significant negative biases in water vapor.

[20] CAM3.5 water vapor biases are small (Figure 1f), and a large overestimation of ozone mixing ratios in excess of 1 ppm near the model upper boundary (Figure 1e), which should lead to overestimated solar heating, seems inconsistent with the CAM3.5 cold bias in this region. Hence the cold bias for this model above 10 hPa is likely to be due to inaccuracies in the model's radiative scheme or possibly associated with the low upper boundary.

[21] CCSRNIES displays the largest bias in water vapor of all models. The model underestimates the observed values by 2–4 ppm in the middle and upper stratosphere, which likely explains a significant fraction of the model's warm bias in this region. CCSRNIES also overestimates ozone near its peak in the middle stratosphere by almost 2 ppm, which should also contribute to the warm bias. Thus, it is possible that the warm bias in the middle stratosphere is due to biases in ozone and water vapor alone, while in the upper stratosphere, where the model simulation of ozone is quite adequate, the water vapor bias is unlikely to be responsible for the entire 8 K bias there. Also, the cold bias in the lower stratosphere and upper troposphere, cannot be linked to biases in ozone and water vapor, and thus is likely due to inaccuracies in the model's radiative scheme.

[22] CMAM displays a similar positive temperature bias to that of CCSRNIES in the middle and upper stratosphere. While CMAM underestimates water vapor by about 1 ppm throughout the stratosphere, which should lead to somewhat underestimated infrared cooling, this can only explain a small fraction of the CMAM warm bias. Furthermore, the

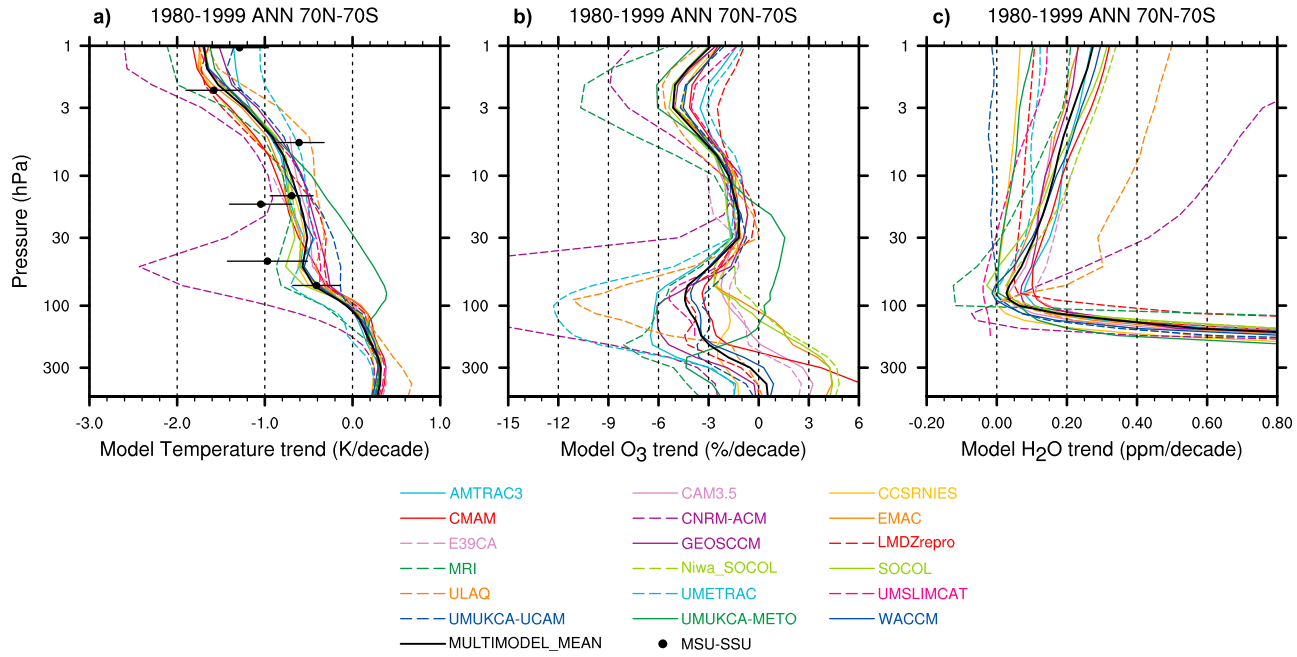


**Figure 2.** Near-global (70°S–70°N) and annual mean trends over 1980–1999 for (a) temperature, (b) ozone, and (c) water vapor ratio, for REF-B1 model simulations. Figure 2a includes satellite observed MSU/SSU trends and 95% confidence intervals. MSU/SSU data points include channels: MSU-4 (at 70 hPa), SSU25 (15 hPa), SSU26 (5 hPa), SSU27 (2 hPa), SSU15X (45 hPa), SSU26X (15 hPa), and SSU36X (1 hPa), where the specified pressure levels represent the approximate weighted mean heights derived from the MSU/SSU vertical weighting functions for each channel [see *Randel et al.*, 2009], negative portions of the weighting functions excluded. The solid black lines indicate the multimodel mean results. For other data sets, see legend. Model acronyms are described in Table 1 and references therein.

fact that CMAM underestimates ozone slightly in this region, which should lead to reduced solar heating, suggests that the CMAM warm bias in this region is likely to be primarily due to inaccuracies in the model's radiative scheme.

[23] CNRM-ACM ozone biases are small, and although a 1 ppm positive bias in water vapor throughout the stratosphere should contribute to a somewhat overestimated infrared cooling, the bulk of the cold bias in this model is likely to be due to inaccuracies in the model's radiative scheme.

[24] LMDZrepro displays similar biases as CMAM, with overestimated upper stratospheric temperatures, a slight low ozone bias in the upper stratosphere, and a negative bias in water vapor throughout the stratosphere. Although the water vapor bias for LMDZrepro is significantly stronger than for CMAM, amounting to 2–3 ppm, this bias is not sufficient to explain the large warm bias in the upper stratosphere. This and the fact that LMDZrepro agrees well with observed temperatures below 5 hPa (despite a large water vapor bias there) suggests that inaccuracies in the model's radiative scheme should be the main cause for the LMDZrepro temperature bias.

[25] UMUKCA-METO and UMUKCA-UCAM overestimates ozone in the lower stratosphere, which should lead to overestimated radiative heating. This provides a plausible explanation for the UMUKCA-METO and UMUKCA-UCAM warm biases in this region, although other effects cannot be ruled out.

### 3.2. Global Mean Temperature Trends: Past

[26] Figure 2 shows near-global mean trends for temperature, ozone and water vapor from 1980 to 1999 for the REF-B1 model experiments. Trends were calculated from linear fits to the annual mean time series from each model. Figure 2a also shows the observed stratospheric temperature trend over this period, indicated by the MSU/SSU data set. The horizontal error bars for MSU/SSU indicate the 95% confidence intervals for the fitted trends. Note that MSU/SSU data are also associated with uncertainty in the vertical due to the vertical distribution of its weighting functions [see *Randel et al.*, 2009]. Here the MSU/SSU data was simply plotted at the weighted mean heights (negative portions of the weighting functions excluded). Since the focus in this analysis is on temperature no observations are included in Figure 2 for ozone and water vapor, and thus the following qualitative assessment will use the multimodel mean as a reference for these species.

[27] The observed temperature trend is associated with emission of greenhouse gases and ozone depleting substances [*Jonsson et al.*, 2009] and is driven radiatively mostly by increases in $CO_2$ and water vapor and decreases in ozone [*Shine et al.*, 2003]. Methane and nitrous oxide have a much smaller effect on stratospheric temperature. All

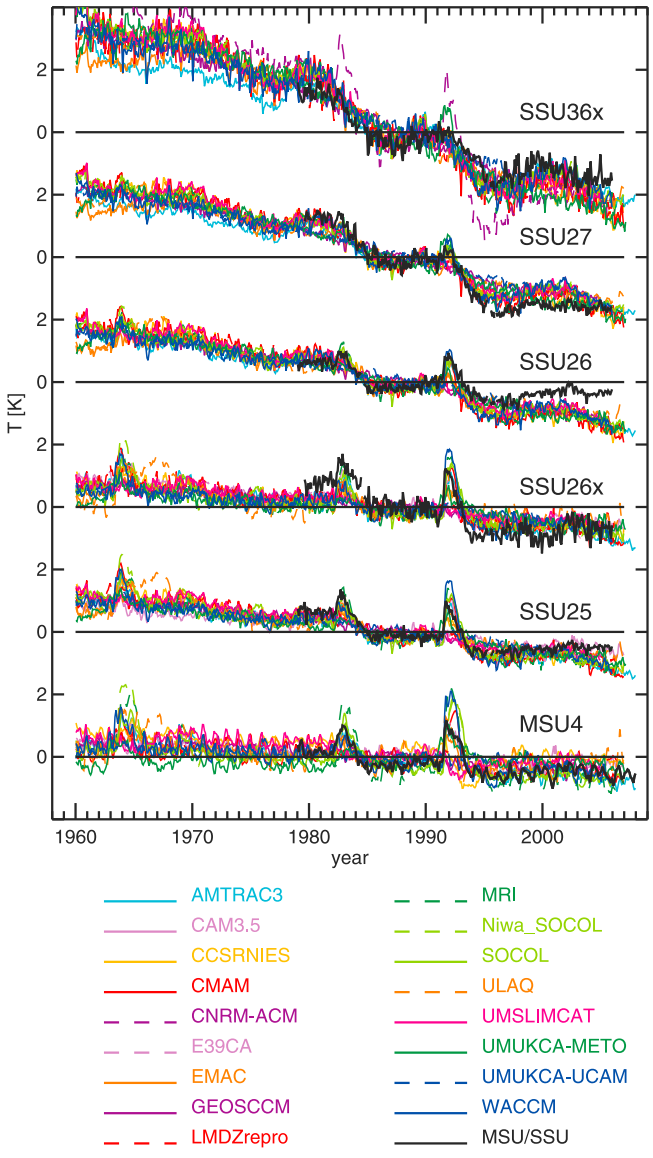


**Figure 3.** Near-global mean time series (70°S–70°N) of MSU/SSU satellite observations and REF-B1 model temperature data weighted by MSU/SSU weighting functions. MSU/SSU channels include: MSU-4 (at 70 hPa), SSU25 (15 hPa), SSU26 (5 hPa), SSU27 (2 hPa), SSU26X (15 hPa), and SSU36X (1 hPa), where the specified pressure levels represent the approximate weighted mean heights derived from the MSU/SSU vertical weighting functions for each channel [see *Randel et al.*, 2009], negative portions of the weighting functions excluded. For each model, only the first ensemble member from the REF-B1 simulations is shown. The anomalies are calculated with respect to the period 1980–1994, as in the provided SSU anomalies. Note that UMETRAC is not included. CNRM-ACM is only shown in the highest SSU36X level due to its too strong sensitivity to volcanoes. UMUKCA-UCAM in not shown after year 2000. Low top models CAM3.5 and E39CA (the lids are at 3 hPa and 10 hPa, respectively) are shown only in the MSU4, SSU25, and SSU26X panels.

models capture the large-scale features of the observed temperature trend, with warming in the troposphere (not shown) and cooling in the stratosphere. Furthermore, the vertical structure of the stratospheric trend, with cooling maxima in the upper and lower stratosphere that are consistent with decreases in ozone (Figure 2b), is generally well captured. Disregarding the main model outliers in the stratosphere, CNRM-ACM and UMUKCA-METO, the model spread varies between 0.4 K/decade and 0.8 K/decade. In the deep troposphere (below 300 hPa) the models agree better, and except for the main outlier there, ULAQ, the model spread is within 0.2 K/decade. The multimodel mean results overlap with, or are very close to overlapping with, the MSU/SSU uncertainty estimates, and the disagreements are largest for the so-called SSU X channels that are not as reliable as the regular SSU channels. Note that many models with significant biases in the temperature climatology (see section 3.1), including CCSRNIES, CMAM, LMDZrepro and CAM3.5, do not show a significant disagreement with the observed trends. Some models, however, and most notably CNRM-ACM and UMUKCA-METO, but also MRI, UMETRAC, UMUKCA-UCAM and ULAQ, display trends that are in sufficient disagreement with the observations and the multimodel mean trend that they warrant some further investigation.

[28] CNRM-ACM overestimates the observed cooling trend throughout most of the stratosphere and exhibits cooling, rather than warming, in the upper troposphere (Figure 2a). The discrepancies are particularly severe near the stratopause and in the lower stratosphere and upper troposphere, between 200 and 20 hPa, where the modeled trend is a roughly factor of 1.5 and 4, respectively, greater than the multimodel mean trend. The overestimated temperature trend is quite clearly associated with a significantly overestimated negative ozone trend (Figure 2b) and a significantly overestimated positive water vapor trend (Figure 2c), both leading to overestimated cooling. A particularly strong temperature response to volcanic eruptions in 1982 an 1991 (Figure 3) appears to be partly responsible for these anomalous trends.

[29] MRI also overestimates the temperature trend near the stratopause and in the lower stratosphere and upper troposphere, although to a lesser degree than CNRM-ACM. This appears to be associated with too strong negative ozone trends.

[30] UMETRAC displays a stronger temperature trend than most models in the upper troposphere and lower stratosphere and a weaker trend than most models in the upper stratosphere. This seems consistent with slightly stronger and weaker ozone trends than most models in these respective regions.

[31] UMUKCA-METO displays an anomalous feature with a weaker than average temperature trend in the middle stratosphere and a positive trend of up to 0.4 K/decade in the lower stratosphere. This behavior seems directly related to an anomalous ozone trend with positive, rather than negative, values throughout the lower and middle stratosphere.

[32] While UMUKCA-UCAM and UMUKCA-METO showed very similar results for the temperature and ozone climatologies and biases (Figure 1) this is not the case for temperature trends. UMUKCA-UCAM performs well throughout the domain, except for a slightly weaker than average trend in the lower stratosphere, which appears

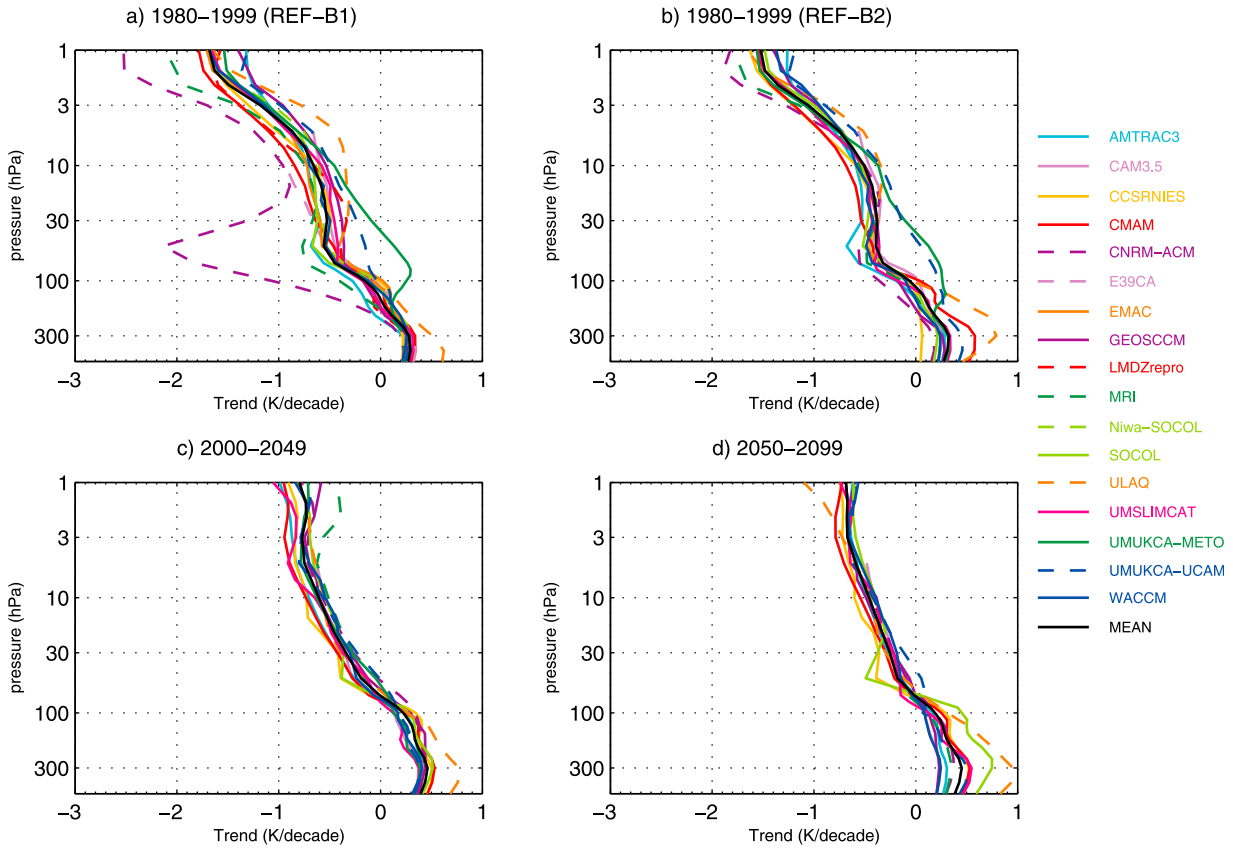


**Figure 4.** Global and annual mean temperature trends from (a) REF-B1 for 1980–1999, and from REF-B2 for (b) 1980–1999, (c) 2000–2049, and (d) 2050–2099. Note that UMETRAC is not included here and that four models shown for REF-B1 (EMAC, E39CA, LMDZrepro, and Niwa_SOCOL) did not supply data for REF-B2. The solid black lines indicate the multimodel mean results. For other data sets, see legend. Model acronyms are described in Table 1 and references therein.

consistent with the absence of a significant negative water vapor trend and a slightly weaker than average negative ozone trend in this region.

[33] ULAQ displays somewhat weaker negative temperature trends than the other models at 20–2 hPa, despite showing reasonable ozone trends in this region and an overestimated water vapor trend. As the latter would lead to more cooling, not less, this suggests that the lower than average sensitivity for this model at 20–2 hPa could be due to inaccuracies in the model's radiative scheme. Also, although the focus here is on the stratosphere, it can be noted that the upper tropospheric warming in ULAQ is much stronger than for other models (by roughly a factor of 2 below 300 hPa). This appears to be related to an upper tropospheric increase in water vapor that is about twice as strong as for the multimodel mean (not shown).

[34] Figure 3 shows the full time series of global mean temperature anomalies compared to satellite data weighted over specific vertical levels [see *Randel et al.* [2009]. Most of the models capture the observed trends and variability. In particular many CCMs capture the leveling of the temperature since the late 1990s. Compared to other levels the simulated temperatures are much closer to the observations in the lower stratosphere (MSU-4 data). This is partly the result of the use of the observed SST by all models. These SSTs control the evolution of mid and upper tropospheric temperatures and the signal from the MSU-4 channel partly comes from these tropospheric levels.

[35] A disagreement between the models and observations is clearly seen in SSU26 over the last decade. SSU26 has a maximum weight at about 5 hPa and a considerable contribution from the lower stratosphere. In contrast the agreement is better in SSU27 which peaks at 2 hPa with less contribution from the lower stratosphere.

### 3.3. Global Mean Temperature Trends: Future

[36] To assess the model simulations of future changes Figures 4c and 4d show global mean vertical temperature trend profiles for 2000–2049 and 2050–2099 for the REF-B2 model experiments. For reference, the global mean trends for 1980–1999 for REF-B1 and REF-B2 are shown in Figures 4a and 4b. We first compare the REF-B2 and REF-B1 results for 1980–1999. The REF-B2 results are generally very similar to the REF-B1 results in the stratosphere, as should be expected since the prescribed changes of GHGs and ODSs are the same in both scenarios. The multimodel mean trends for REF-B1 and REF-B2 are very close. However, there are a few important differences that are discussed below.

[37] While the focus here is on the stratospheric results it can be noted that three models show significantly different temperature trends in the upper troposphere for REF-B2 than for REF-B1. CMAM and UMUKCA-UCAM REF-B2 trends are roughly 2 and 1.5 times as strong as the multimodel mean trend in this region. For CMAM this is related to its coupled ocean implementation. CCSRNIES shows the opposite behavior, i.e., underestimating the multimodel trend, showing a near-zero trend throughout the troposphere for REF-B2.

[38] For the stratosphere the REF-B2 trends show slightly better agreement between the various models than for REF-B1 (but note that not all models provided data for REF-B2). This is not surprising as the variation in model response to volcanic eruptions and solar variability contributes to different temperature responses in the REF-B1 simulations, while those effects are not considered for REF-B2.

[39] CNRM-ACM shows the most dramatic difference in temperature trends between REF-B1 and REF-B2 of all models. The considerably overestimated cooling trends for 1980–1999 for REF-B1 are much reduced in REF-B2, particularly in the lower stratosphere. This confirms the earlier speculations that the CNRM-ACM temperature trend biases for REF-B1 are largely due to effects of volcanic eruptions, since the REF-B2 simulation does not include those. It can be speculated that the particularly large model spread for REF-B1 in the lower stratosphere, including significant deviations also for MRI, UMETRAC, UMUKCA-METO and UMUKCA-UCAM, could be related to different responses to volcanic eruptions. Note that for REF-B2, except for UMUKCA-METO and UMUKCA-UCAM the model spread is quite small. Further work is needed to understand this better. MRI shows better agreement with the multimodel mean for REF-B2 than for REF-B1, particularly in the upper troposphere and lower stratosphere. UMUKCA-UCAM on the other hand showed better agreement with the multimodel mean (and with the observations) for REF-B1 than for REF-B2. For REF-B2, UMUKCA-UCAM follows the anomalous results of UMUKCA-METO, showing a strong positive bias in its temperature trend throughout the lower and middle stratosphere.

[40] The future global mean temperature trend is attributable primarily to $CO_2$ increase, although the expected gradual recovery of ozone over the 21st century will reduce the $CO_2$ induced cooling somewhat in the upper stratosphere [*Jonsson et al.*, 2009]. A hint of this can be seen in Figures 4c and 4d. For 2000–2049 (Figure 4c) only two models can be considered as significant outliers: MRI underestimates the multimodel cooling trend in the upper stratosphere and ULAQ overestimates the multimodel warming trend in the upper troposphere. In particular the anomalous behavior of UMUKCA-METO and UMUKCA-UCAM in the lower stratosphere is not present in this period. CMAM and UMUKCA-UCAM tropospheric trends are also closer to the multimodel mean trend. MRI did not include $CH_4$ changes after 2002 which would explain weaker temperature trend for MRI in the upper stratosphere than for other models ($CH_4$ is the main source of upper stratospheric water vapor and odd hydrogen that control ozone loss rates in this region). For 2050–2099 (Figure 4d) the same level of agreement between the models is achieved in the stratosphere. In the troposphere, however, the model spread is larger during 2050–2099 than during 2000–2049. In particular, SOCOL shows a more anomalously warm trend during 2050–2099 than during 2000–2049.

## 4. Evaluation of the CCM Radiation Codes Performance

[41] There is a long history of international efforts aimed on the evaluation of the radiation codes of climate models. After several national projects in Europe, Russia and United States [e.g., *Feigelson and Dmitrieva*, 1983; *Luther et al.*, 1988] the first international comparison of radiation codes for climate models (ICRCCM) campaign was launched in 1984. ICRCCM resulted in a series of publications [*Ellingson et al.*, 1991; *Fouquart et al.*, 1991] which evaluated the performance of the existing radiation codes and inspired further progress. ICRCCM also established a framework for the subsequent campaigns, which is based on the comparison of the radiation codes against reference high-resolution LBL codes. This approach was justified by unavailability of reliable observations of the radiation fluxes and heating rates in the atmosphere. There were several other attempts to evaluate radiation codes for climate models. The representation of clouds was analyzed by *Barker et al.* [2003] An evaluation of clear sky radiation codes used by IPCC AR4 GCMs was performed by *Collins et al.* [2006], employing a single profile and solar zenith angle. These evaluations were also based on the comparison of operational radiation codes with reference LBL schemes. Such tests can provide a useful, if incomplete, understanding of potential sources of uncertainty and error, because the state-of-the-art LBL radiation codes are used as a base for the judgment. A more complete picture can be obtained by comparing radiation codes directly implemented to a single climate model [e.g., *Feigelson and Dmitrieva*, 1983; *Cagnazzo et al.*, 2007]. However, it would not be feasible to apply this approach using the LBL reference codes due to their high computational costs and, moreover, the results of off-line experiments allow clear evaluation of the model performance and interpretation of the underlying causes of error.

[42] Most of the previous campaigns were aimed at the radiation fluxes and tropospheric heating/cooling rates evaluation. In this comparison we focus on two aspects of radiation code output: stratospheric heating/cooling rates and instantaneous radiative fluxes. The heating/cooling rates are necessary to understand the biases and trends in the global mean stratospheric temperature, while the instantaneous radiative fluxes can help to interpret global climate change, including surface temperature change. It should be noted that the evaluation of radiation codes in cloudy conditions and in the presence of different atmospheric aerosols will not be performed here, because of high uncertainties in aerosol optical properties and limited availability of proper reference codes. Nevertheless, these issues are very important and should be addressed in the future work.

[43] In this section we analyze the performance of the CCM radiation codes presented in section 2 using the results of off-line calculations. Section 4.1 describes the cases required for this analysis. Sections 4.2 and 4.4 evaluate the performance of CCM radiation codes for the control case (case A; see section 4.1), for fluxes and heating/cooling

**Table 3.** Offline Radiation Experiments Undertaken

| Case | Details |
|---|---|
| A | 1980 Control experiment |
| B | $CO_2$ from 338 ppm to 380 ppm |
| C | $CH_4$ from 1600 ppb to 1750 ppb |
| D | $N_2O$ from 300 ppb to 320 ppb |
| E | CFC-11 from 150 ppt to 250 ppt |
| F | CFC-12 from 300 ppt to 550 ppt |
| G | All long-lived greenhouse gas changes combined (B-F) |
| H | 10% stratospheric ozone depletion, for pressures less than 150 hPa |
| I | 10% tropospheric ozone increase, for pressures greater 150 hPa |
| J | 10% stratospheric water vapor increase, for pressures less than 150 hPa |
| K | 10% tropospheric water vapor increase, for pressures greater than 150 hPa |
| L | Combined stratospheric ozone depletion and greenhouse gas changes (G and H) |

rates, respectively, which can help to explain the possible causes of the biases in the CCM simulated climatological temperature discussed in section 3. Sections 4.3 and 4.5 evaluate the response of the simulated radiation fluxes and heating rates, respectively, to the changes of atmospheric gas composition, and section 4.6 discusses the effect of errors in heating rates and distribution of ozone and water vapor on biases in the global mean temperature climatology.

### 4.1. Experimental Setup

[44] We perform a number of clear sky and aerosol free tests using zonally averaged profiles of the atmospheric state parameters compiled from ECMWF ERA-40 reanalysis data [*Uppala et al.*, 2005] and ozone data provided by *Randel and Wu* [2007]. These profiles represent January atmosphere and are given for five latitudes (80°S, 50°S, 0°, 50°N, and 80°N). The solar fluxes in the atmosphere were calculated for three solar zenith angles, allowing one to evaluate the radiation code performance for diurnal means as well as for different solar positions. Where possible the extraterrestrial spectral solar irradiance was prescribed with ~1 nm resolution from *Lean et al.* [2005] compilation. Surface albedo was set to 0.1 for all cases. We also asked participants to use solar irradiance for 1 AU Sun-Earth distance. The set of reference vertical profiles and the description of the test cases are presented at www.env.leeds.ac.uk/~piers/ccmvalrad.shtml. These tests were designed to very crudely approximate the radiative forcing evolution since 1980 due to ozone and greenhouse gases. The descriptions of all CCMs and their acronyms have been presented by *Morgenstern et al.* [2010]. Table 3 describes the experiments undertaken. Case A represents the control experiment and is based on the concentration of radiatively active species for 1980. The cases B-L are based on the observed changes of gas abundances in the atmosphere from 1980 to 2000 and allow us to evaluate the radiation code response to these climate forcings.

[45] As a base for comparison we use the results of five LBL codes: AER [*Clough and Iacono*, 1995; *Clough et al.*, 2005]; FLBLM [*Fomin and Mazin*, 1998; *Fomin*, 2006; *Halthore et al.*, 2005]; LibRadtran [*Mayer and Kylling*, 2005]; NOAA [*Portmann et al.*, 1997] and OSLO [*Myhre and Stordal*, 1997, 2001; *Myhre et al.*, 2006]. AER, FLBLM, NOAA and OSLO provided longwave (LW) fluxes, while shortwave (SW) fluxes were calculated with FLBLM, LibRadtran and OSLO codes. Therefore for most of the cases the results of at least three independent LBL codes are available. We treat the results from the LBL codes equal likely and the uncertainty range provided by the LBL models are used for the description of the CCM codes. The complete set of the test calculations was submitted by the following thirteen CCMs: AMTRAC3, CCSRNIES, CMAM, E39CA, EMAC, GEOSCCM, LMDZrepro, MRI, SOCOL, NIWA-SOCOL (which is identical to SOCOL), UMSLIMCAT, UMUKCA_METO, and UMUKCA_UCAM. Five CCMs (CAM3.5, CNRM-ACM, ULAQ, UMETRAC, and WACCM) did not participate in the radiation code comparison. Two CCMs have radiation codes based on ECHAM4 (E39CA and SOCOL). In addition to the operational codes we also analyzed the results of four prospective radiation codes: ECHAM5, LMDZ-new, UKMO-HADGEM3 and UKMO-Leeds, which will be used in the new generation of CCMs or GCMs.

### 4.2. Fluxes: Control Experiment

[46] The global and diurnal mean net (downward minus upward) LW, SW and total (SW+LW) fluxes for case A calculated with AER (LW) and LibRadtran (SW) at 200 hPa (the pseudotropopause) are presented in the "A (reference trop)" entry in Table 4. The differences between the fluxes calculated with all participating models and two particular LBL codes (AER for LW and LibRadtran for SW) at the pseudotropopause are illustrated in Figure 5. For this particular case the accuracy of the calculated SW fluxes is very good. The scatter among the LBL codes is within 1 W/m$^2$. Most of the participating CCMs show a net SW flux error smaller than 2.5 W/m$^2$. Only the SW radiation scheme of MRI produces a larger error, ~4 W/m$^2$. For LW and total radiation the situation is slightly worse. While LBL codes are in a very good agreement, total flux errors for GEOSCCM, LMDZrepro and CCSRNIES exceed 4 W/m$^2$, primarily due to errors in LW calculations. MRI and UMSLIMCAT also display a total flux error of ~4 W/m$^2$, which is due to either SW errors (for MRI) or a combination of SW and LW errors (for UMSLIMCAT). In general, an

**Table 4.** Global and Diurnal Mean Net LW, SW, and Total (LW +SW) Fluxes for Case A and Their Deviation for Cases B–N From Reference Case A at the Pseudotropopause Calculated With AER (LW) and LibRadtran (SW)

| Case | LW Flux (W/m$^2$) | SW Flux (W/m$^2$) | Total Flux (W/m$^2$) |
|---|---|---|---|
| A (reference surface)[a] | −71.88 | 223.77 | 151.89 |
| A (reference trop) | −234.076 | 282.444 | 48.368 |
| B ($CO_2$) | 0.815 | −0.052 | 0.763 |
| C ($CH_4$) | 0.072 | −0.006 | 0.066 |
| D ($N_2O$) | 0.073 | −0.0026 | 0.0704 |
| E (CFC-11) | 0.0251 | 0.0 | 0.0251 |
| F (CFC-12) | 0.078 | 0.0 | 0.078 |
| G (LLGHG) | 1.063 | −0.061 | 1.002 |
| H ($O_3$ strat) | −0.094 | 0.34 | 0.246 |
| I ($O_3$ trop) | 0.164 | 0.006 | 0.170 |
| J ($H_2O$ strat) | 0.072 | −0.013 | 0.059 |
| K ($H_2O$ trop) | 2.258 | 0.089 | 2.347 |
| L (LLGHG&$O_3$) | 0.971 | 0.278 | 1.248 |

[a]Surface fluxes shown for reference.

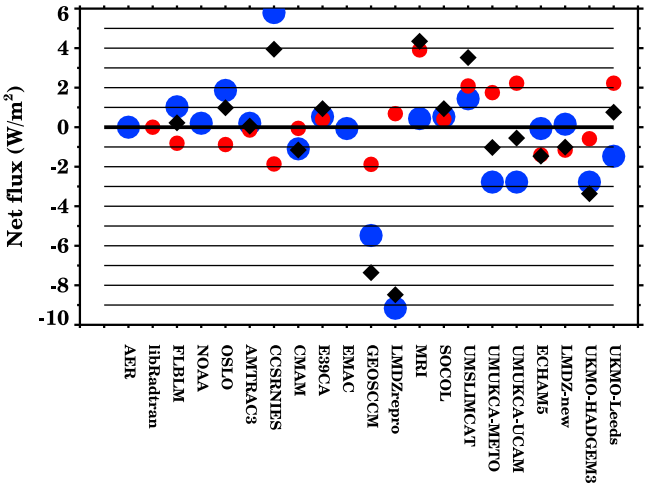


**Figure 5.** The global and diurnal mean SW (red circles), LW (blue circles), and total (black diamonds) net flux deviations from the LBL code (AER for LW and libRadtran for SW) at the model pseudotropopause (200 hPa).

error of ~4 W/m$^2$ could lead to ~4 K error in the global mean surface temperature, unless this error is compensated by some other bias in the concentrations of radiatively active gases or physical parameterizations in the core CCM. It is interesting to note, that for UMUKCA_METO, UMUKCA_UCAM and UKMO-Leeds the SW and LW errors compensate each other making the model performance for the total net flux better than for its individual components. From the presented results it can be concluded that the performance of the majority of participating models in the simulation of the net fluxes at the pseudotropopause is very good.

[47] The global and diurnal mean net (downward minus upward) LW, SW and total (SW+LW) fluxes for case A calculated with AER (LW) and LibRadtran (SW) at the surface are presented in the "A (reference surface)" entry in Table 4. Deviations from the LBL code are shown in Figure 6. In general, the model accuracy at the surface is similar to the results at the pseudotropopause for LW fluxes. All models except the ECHAM4 family of models (E39CA and SOCOL), CMAM, LMDZrepro and CCSRNIES have relatively small (<2 W/m$^2$) biases.

[48] Figure 7 illustrates the errors in downward LW fluxes simulated with three of these models relative to the reference AER LBL scheme. The SOCOL radiation scheme overestimates the downward LW flux at the surface by more than 7.5 W/m$^2$, which leads to an overestimation of the net LW flux, because the upward LW flux is constrained by the prescribed surface temperature and emission efficiency. The overestimation of the downward flux in SOCOL starts from ~250 hPa and its magnitude increases toward surface, which suggests some problems with the emission by water vapor or its continuum in the atmospheric transparency window. Similar behavior (perfect agreement in the stratosphere and rising overestimation in the troposphere) is also characteristic for the CCSRNIES model down to ~300 hPa, however, in the lower troposphere CCSRNIES dramatically underestimates LW downward fluxes, which leads to substantial errors at the surface and potential implications for the surface energy budget in the core CCM. This model deficiency can be connected to some problems in the representation of the strong emission from $H_2O$ rotational ($\lambda > 15$ $\mu$m) or vibrational (~6.3 $\mu$m) bands. The accuracy of the LMDZrepro LW downward flux is reasonable in the stratosphere and upper troposphere, but in the lower troposphere and at the surface the model error exceeds 5 W/m$^2$. This model also generates a step like change in the downward LW fluxes around 10 hPa.

[49] The accuracy of the calculated SW net fluxes at the surface (Figure 6) is generally not as good as at the pseudotropopause. For this case only six models (AMTRAC3, CCRSNIES, GEOSCCM, ECHAM5, LMDZ-new and UKMO_HADGEM3) perform well. All other models are biased high compared to the reference LibRadtran results. The magnitude of the bias varies from about 5 to 8 W/m$^2$ with larger biases for the ECHAM4 family, CMAM, LMDZrepro and MRI. The bias in the SW net fluxes mostly comes from the errors in the downward SW fluxes, because the upward SW fluxes are smaller and constrained by the prescribed surface albedo. The downward SW flux errors in most of the above-listed models have similar behavior. As illustrated in Figure 8 the errors are small in the stratosphere, but start to increase around ~200 hPa reaching the maximum value near the surface. Because the main absorber of the solar irradiance in the cloud and aerosol free troposphere is water vapor, it can be tentatively concluded that $H_2O$ absorption in the near-infrared spectral region is underestimated by these models, although underestimating $O_3$ absorption in the visible spectral region also can contribute. The errors in the total net radiation fluxes (Figure 6) coincide with the errors in SW net fluxes for most of the models. The exceptions are ECHAM4 family of models, LMDZrepro and CCSRNIES. In ECHAM4 based models the errors in SW and LW net fluxes are almost equal in magnitude providing a substantial deviation of the surface radiation balance from the reference results. The total net flux error for CCSRNIES is very large (~30 Wm$^{-2}$) and is dominated by the problems in the LW part of the code. The error in

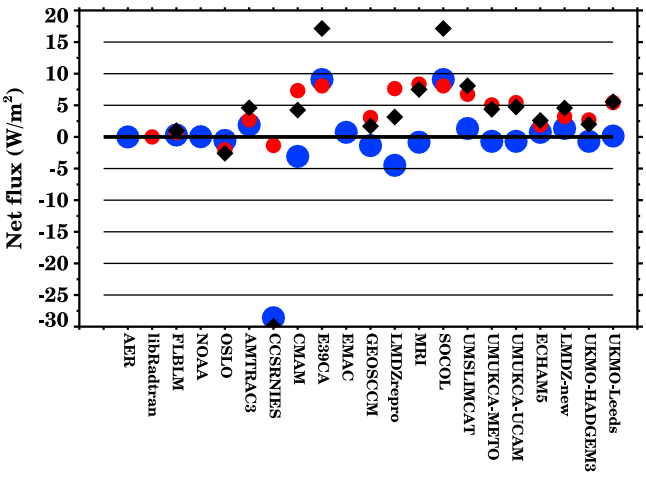


**Figure 6.** The global and diurnal mean SW (red circles), LW (blue circles), and total (black diamonds) net flux deviations from the LBL code (AER for LW and libRadtran for SW) at the surface.

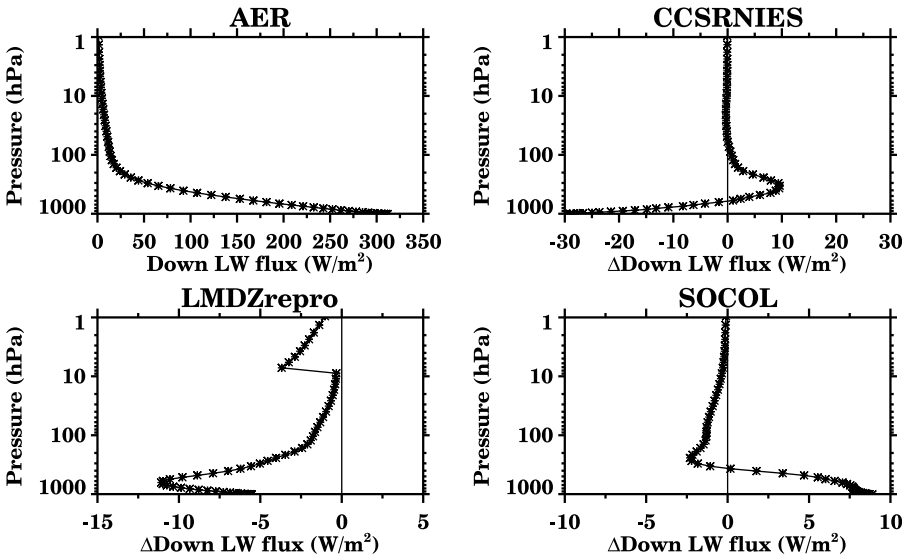


**Figure 7.** The vertical profiles of the global LW downward flux from the LBL code (AER) and the absolute deviations of SOCOL, LMDZrepro, and CCSRNIES results from the reference AER LBL scheme.

total net surface flux for LMDZrepro is rather small due to compensation of the errors in SW and LW calculations.

### 4.3. Fluxes: Sensitivity Experiments

[50] The analysis of the radiation flux responses to the observed changes of gas abundances in the atmosphere from 1980 to 2000 is an important part of the radiation code evaluation, because the accuracy of past climate change simulations depends on the ability of the radiation codes to properly simulate the effects of the main climate drivers [*Collins et al.*, 2006]. In Table 4 we present the near-global and diurnal mean net LW, SW and total flux changes for cases B-L relative to reference case A (for case definitions see Table 3) at the pseudotropopause simulated with reference LBL codes (AER for LW fluxes and LibRadtran for SW fluxes). The calculated effects of different atmospheric perturbations are generally close to previous estimates [e.g., *Collins et al.*, 2006; *Forster et al.*, 2007].

[51] The global and diurnal mean net SW, LW and total flux deviations of the radiative forcing due to $CO_2$ increase relative to the results of the LBL codes at the pseudotropopause are presented in Figure 9. The accuracy of the LW radiation codes is generally very good and is within 10% for most of the participating models. Slightly larger underestimation of the $CO_2$ forcing is visible for the ECHAM4 family, CMAM and LMDZrepro, but it does not exceed 20%.

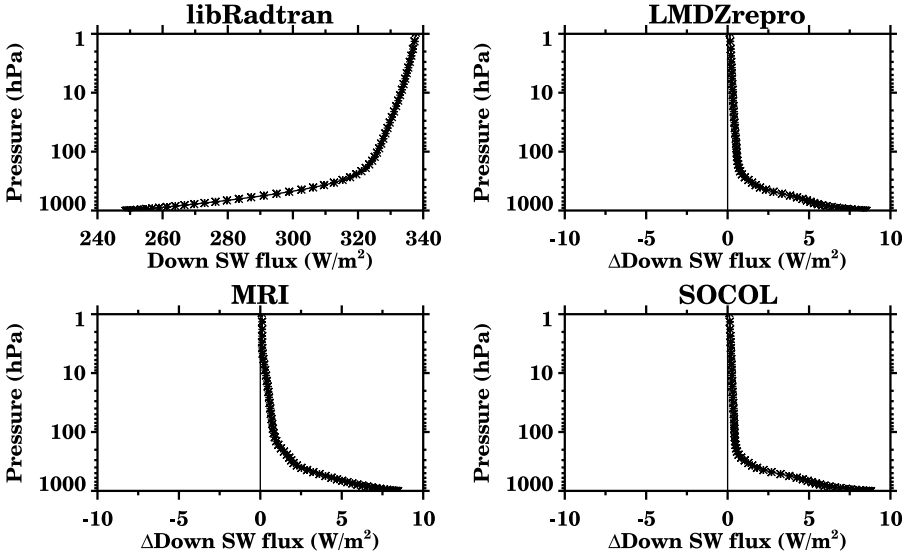


**Figure 8.** The vertical profiles of the global and diurnal mean SW downward flux from the LBL code (libRadtran) and the absolute deviations of SOCOL, MRI, and LMDZrepro results from the reference libRadtran LBL scheme.

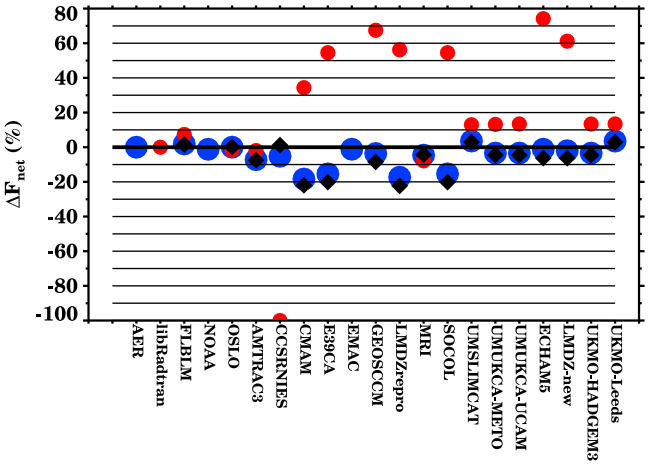


**Figure 9.** The global and diurnal mean SW (red circles), LW (blue circles), and total (black diamonds) net flux deviations of the radiative forcing due to $CO_2$ (case B) increase relative to the results of LBL codes (AER for LW and libRadtran for SW) at the pseudotropopause.

[52] The relatively weak SW solar $CO_2$ forcing is more difficult to simulate. Only the AMTRAC3 and MRI results are in good agreement with the reference code, while most of the models (except CCSRNIES) overestimate its magnitude. The accuracy is still reasonable (<20%) for the UKMO family of models (UMSLIMCAT, UMUKCA-METO, UMUKCA-UCAM, UKMO-HADGEM3 and UKMO-Leeds), but several other models overestimate the solar $CO_2$ forcing by up to 80%. CCSRNIES does not include $CO_2$ in the solar part of the code and therefore underestimates SW forcing by 100%. The total (SW+LW) forcing is dominated by LW forcing. Therefore the accuracy of the total forcing calculation almost completely coincides with the accuracy of LW forcing. Similar conclusions can be drawn for the accuracy of radiative forcing due to increase of all long-lived greenhouse gases (LLGHG) (Figure 10) since the

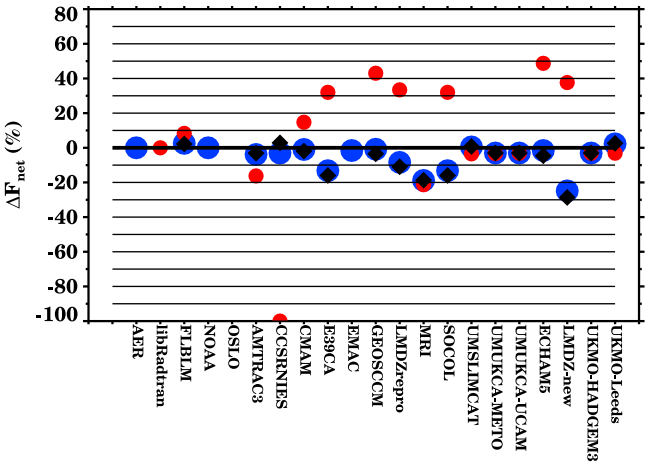


**Figure 10.** The global and diurnal mean SW (red circles), LW (blue circles), and total (black diamonds) net flux deviations of the radiative forcing due to LLGHG (case G) increase relative to the results of LBL codes (AER for LW and libRadtran for SW) at the pseudotropopause.

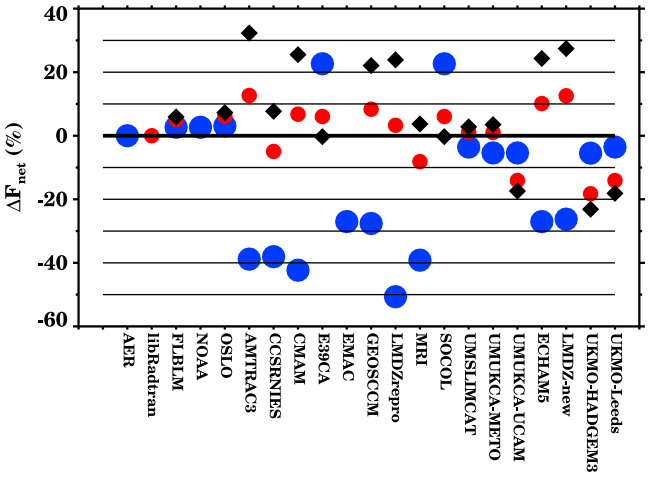


**Figure 11.** The global and diurnal mean SW (red circles), LW (blue circles), and total (black diamonds) net flux deviations of the radiative forcing due to stratospheric ozone depletion (case H) relative to the results of LBL codes (AER for LW and libRadtran for SW) at the pseudotropopause.

forcing magnitude is mostly defined by the $CO_2$ increase. However, for this case the accuracy of the LW forcing calculations is slightly lower for MRI and LMDZ-new and much higher for CMAM. It can be explained by the error compensation in the latter model, which underestimates LW $CO_2$ forcing but overestimates the LW forcing by $N_2O$ and CFCs (see Table 4). It should be noted, that the CCSRNIES code does not take into account all LLGHG in the solar part of the spectrum (Tables 2a and 2b).

[53] Figure 11 shows the accuracy of the considered radiation codes for case H (10% decrease of stratospheric ozone). In contrast to the previously considered cases the SW forcing for this case plays a major role and all models are able to simulate its magnitude with an accuracy of 20% or better. The performance of some models in the LW part, however, is poor. The accuracy of AMTRAC3, CCSRNIES, CMAM, EMAC, GEOSCCM, LMDZrepro, MRI, ECHAM5 and LMDZ-new is only around 30% or worse, which has important implications for the total forcing of stratospheric ozone.

[54] The accuracy of the LW radiative forcing due to tropospheric ozone and water vapor increase (cases I and K, not shown) is within 10% for all models except CCSRNIES, which has a problem with the $H_2O$ treatment in the LW part of the spectrum and underestimates the LW forcing for case K by ~20%. The solar forcing for these cases does not play a substantial role. The results for the case J (stratospheric water vapor increase) are shown in Figure 12. For this case it is interesting to note ~100% overestimation of the LW stratospheric water vapor forcing by all models from the UKMO family and by ~200% by CCSRNIES. Also among the LBL codes the differences are significant (90% for SW and 40% for LW). The large spread in stratospheric water vapor forcings was also noticed by *Myhre et al.* [2009]. It is even more interesting that the SW forcing by stratospheric water vapor is also roughly two times higher in the UKMO family (except for UMSLIMCAT) than for the reference model.

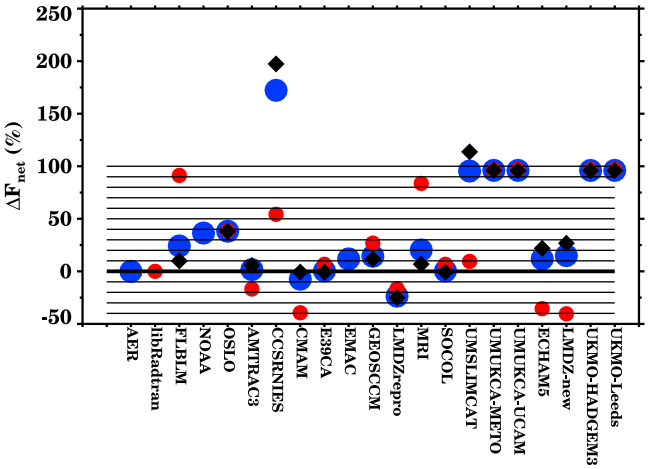


**Figure 12.** The global and diurnal mean SW (red circles), LW (blue circles), and total (black diamonds) net flux deviations of the radiative forcing due to stratospheric water vapor increase (case J) relative to the results of LBL codes (AER for LW and libRadtran for SW) at the pseudotropopause.

[55] The accuracy of the forcing calculations for case L (all LLGHG and stratospheric ozone depletion) is illustrated in Figure 13. This forcing represents the sum of the main climate drivers (except water vapor and tropospheric ozone) for the considered period and its reasonable accuracy is a prerequisite for successful simulation of tropospheric climate changes. The results reveal that most of the models have accuracy of forcing calculations within 10%. The outliers are ECHAM4 based models, LMDZ-new and MRI, which underestimate the total forcing by more than ~10%.

### 4.4. Heating/Cooling Rates: Control Experiment

[56] In this section vertical profiles of total clear sky global mean SW heating rates (diurnally averaged) and LW cooling rates for the relevant cases are discussed. Figure 14 (top) shows global mean SW heating rates for the control case (case A) and their deviations with respect to LibRadtran. Figure 15 (top) shows global mean LW cooling rates for case A and their deviations with respect to AER. Results are discussed for three specific levels located in the lower (70 hPa), middle (15 hPa) and upper (2 hPa) stratosphere. These levels are similar to those at which the observed temperature trends are available (section 3.2).

[57] From Figure 14 it is evident that the correlations among the SW heating rate profiles in the stratosphere are very high, mainly due to the fact that heating rate patterns strongly depend on the gases input profiles, identical for all the models.

[58] For case A, SW heating rate calculations from two sophisticated LBL models other than LibRadtran are available, namely OSLO and FLBLM. OSLO SW heating rates are in better agreement with LibRadtran below 2 hPa (see Figure 14). In particular, FLBLM SW heating rate biases at 70 hPa and 15 hPa are larger than for the OSLO model. However, it is not possible to say which LBL model is the most accurate.

[59] At 2 hPa, most of the models tend to overestimate the LibRadtran SW heating rates. Specifically, the biases found for LMDZ-new (15%), CMAM (9%), UMUKCA-UCAM (9%), the two UKMO models (8%) and ECHAM5 (8%) are more than a factor of two larger than the FLBLM bias (~0.18 K/d). The error at this level is consistent with an overestimation of the ozone solar heating (case H minus case A, the instantaneous change from 10% stratospheric ozone depletion). For case H these models report the largest negative bias of all models at 2 hPa (not shown), indicating a too large sensitivity to the ozone changes. For case A only three models present a negative bias in the SW heating rates larger than 0.18 K/d at this level (E39CA, LMDZrepro, SOCOL) even though they overestimate the ozone heating. This underestimation of the heating rate around the stratopause is however consistent with an underestimation of the $CO_2$ SW heating (case B minus case A, the instantaneous change due to $CO_2$ increase from 338 ppmv to 380 ppmv). However, it should be noted that the LibRadtran SW heating rates at these heights cannot be considered a good benchmark due to the differences between the LBL schemes.

[60] In the middle stratosphere (15 hPa), a better agreement is found between the models and LibRadtran, with all the models in a closer agreement with LibRadtran than with FLBLM.

[61] In the lower stratosphere (70 hPa), most models (except CCSRNIES and GEOSCCM) show a smaller bias with respect to LibRadtran than with respect to FLBLM. In this region, the long radiative relaxation time in the lower stratosphere allows small heating and cooling rate changes to induce substantial temperature changes, therefore a heating/cooling rate bias of few tenths of a degree per day would be able to potentially warm or cool the lower stratosphere by several degrees. Specifically, for GEOSCCM the positive SW heating rate bias is consistent with an overestimation of the ozone absorption.

[62] Figure 15 (top) illustrates global mean LW cooling rates for case A and their deviations with respect to AER. Note that the cooling rate is defined to be a positive quan-

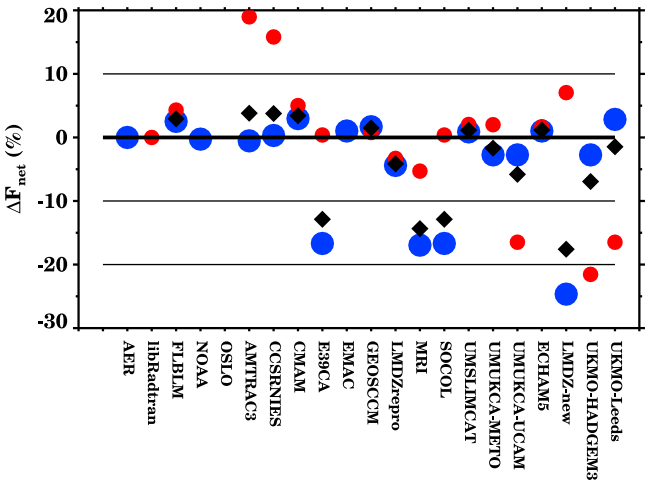


**Figure 13.** The global and diurnal mean SW (red circles), LW (blue circles), and total (black diamonds) net flux deviations of the radiative forcing due to LLGHG and stratospheric ozone changes (case L) relative to the results of LBL codes (AER for LW and libRadtran for SW) at the pseudotropopause.

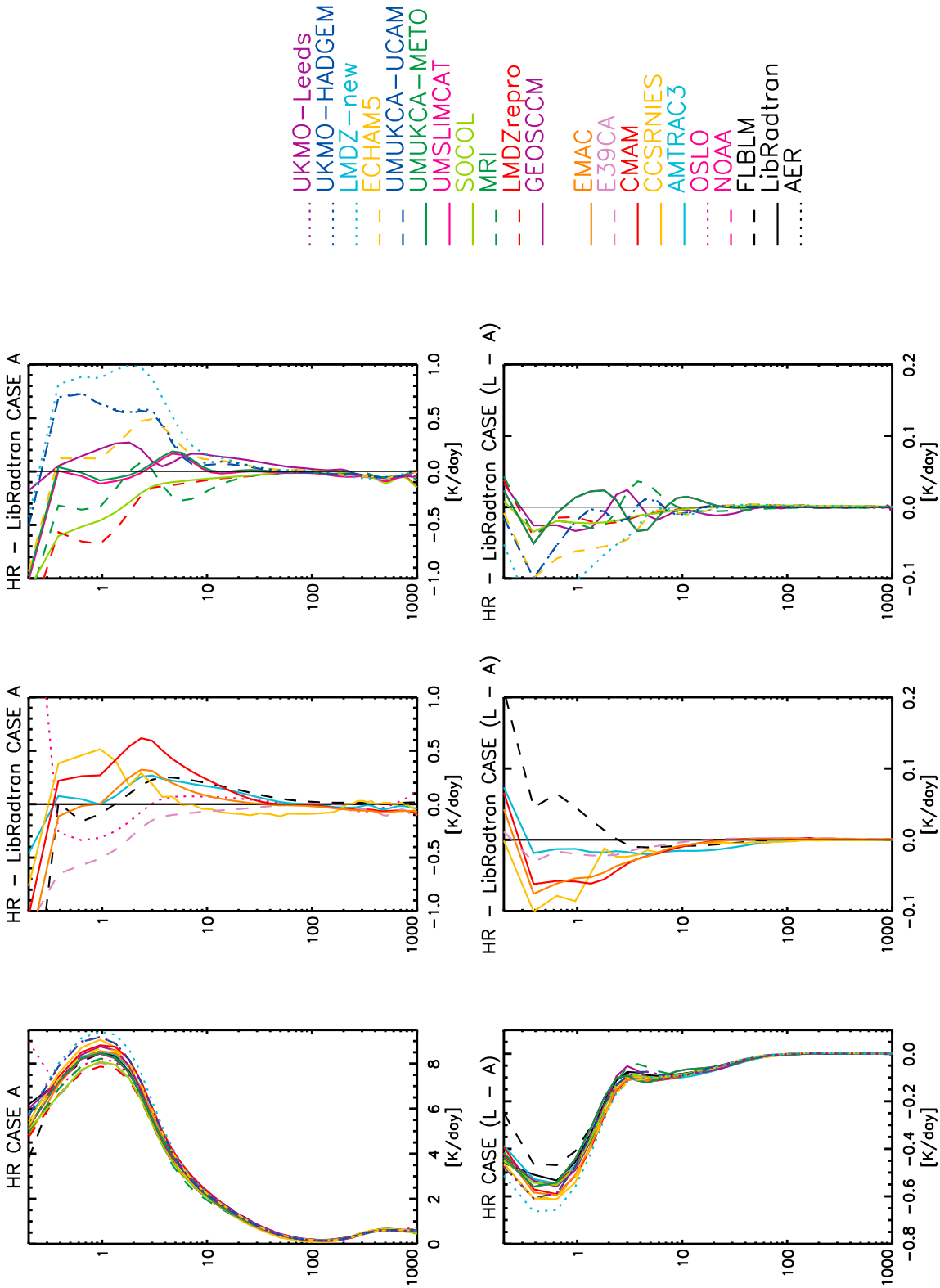


**Figure 14.** (top) (left) The globally averaged shortwave heating rates for case A (control) and (middle and right) differences in this heating rate from that calculated with the LibRadtran. (bottom) (left) The globally averaged shortwave heating rate changes for case L minus case A (the instantaneous change from combined 10% stratospheric ozone depletion and 1980–2000 long-lived greenhouse gas changes) and (middle and right) differences of the same heating rate change from that calculated with the LibRadtran.

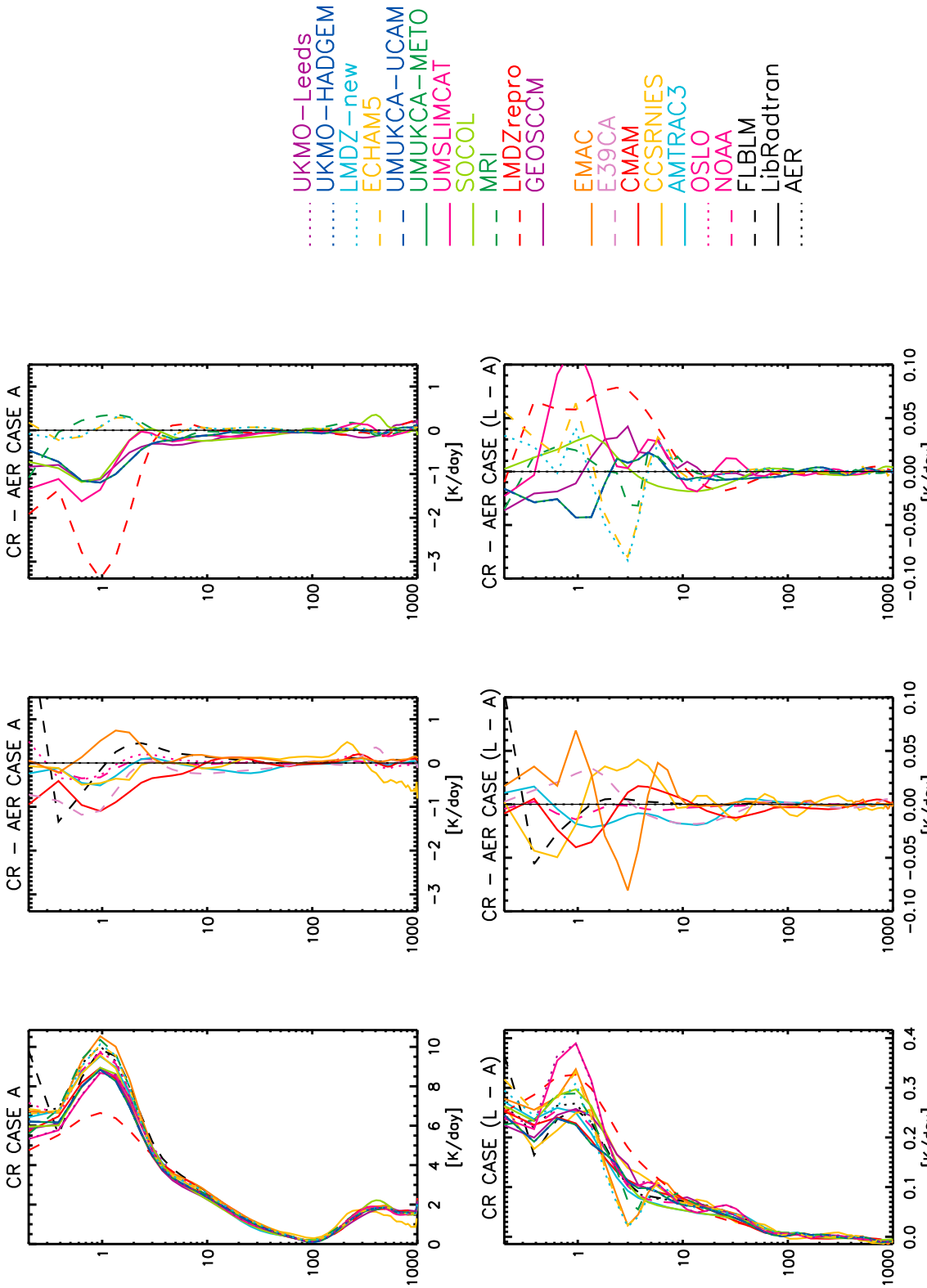


**Figure 15.** (top) (left) The globally averaged longwave cooling rates for case A (control) and (middle and right) differences in this cooling rate from that calculated with the AER model. (bottom) (left) The globally averaged longwave cooling rate changes for case L minus case A (the instantaneous change from combined 10% stratospheric ozone depletion and 1980–2005 long-lived greenhouse gas changes) and (middle and right) differences of the same cooling rate change from that calculated with the AER model.

tity. The strong cooling peak in the upper stratosphere at about 1 hPa is due to the radiative effects of $CO_2$ and, to a lesser degree, $O_3$ and $H_2O$. At 1 hPa, the majority of the models underestimate the cooling rate with a maximum negative bias of more than 3 K/d (LMDZrepro). As for the SW heating rates, the correlations among the LW cooling rate profiles in the stratosphere are high.

[63] Cooling rates from four LBL models are available for case A: AER, FLBLM, NOAA and OSLO. In the lower stratosphere (70 hPa), the biases for FLBLM, NOAA and OSLO with respect to AER are negative and smaller than the biases for the CCMs, with the exception of MRI, GEOSCCM and EMAC. The largest bias is found for CCSRNIES, which is partly due to an overestimation of the $CO_2$ and $H_2O$ cooling rates. At 2 hPa, LMDZrepro, EMAC and CMAM present a larger bias than the bias of FLBLM, consistent with a too high sensitivity to $CO_2$ cooling.

### 4.5. Heating/Cooling Rates: Sensitivity Experiments

[64] Figure 14 (bottom) report the SW heating rate profiles and their biases with respect to LibRadtran for case L (the instantaneous change from combined 10% stratospheric ozone depletion and 1980–2000 long-lived greenhouse gas changes). The LibRadtran profile shows a decreased SW heating rate with respect to case A, with a maximum above 1 hPa of ~−0.6 K/d, almost entirely due to ozone change. Between 1 hPa and 0.2 hPa the majority of the models overestimate the cooling associated with imposed ozone depletion (maximum 25%, LMDZ-new). However, it should be noted that the LBL calculations presented here cannot be considered accurate at these heights due to the strong non-LTE effects for $O_3$ and $CO_2$ solar heating in the mesosphere [e.g., *Fomichev*, 2009].

[65] In the middle and upper stratosphere, almost all the models are too sensitive to the imposed ozone change (negative biases), with a better agreement at 15 hPa (the maximum overestimation at this level is found for AMTRAC3) and larger biases at 2 hPa (maximum biases are found for LMDZ-new, ECHAM5 and CMAM). The maximum SW heating rate biases for reduced ozone at 2 hPa implies a bias in the temperature change of about 0.35 K (see section 4.6). At 70 hPa AMTRAC3 and GEOSCCM are too sensitive to ozone reduction.

[66] The second and third largest heating rate changes in the stratosphere are found for increased $CO_2$ from 338 to 380 ppm (case B) and 10% stratospheric water vapor increase (case J). The absorption of solar radiation by $CO_2$ in the near-infrared spectrum contributes to atmospheric heating of the entire atmosphere, maximizing in the upper stratosphere and mesosphere [e.g., *Fomichev*, 2009]. The LibRadtran vertical profile shows positive heating rate changes in the entire atmosphere, with values ranging between +0.3% above 10 hPa and +0.6% between 100 and 10 hPa due to $CO_2$ increasing (not shown). The majority of contributing models overestimate the absorption of near-infrared radiation below 4 hPa. From analysis of other cases it is evident that none of the models consider absorption in the SW spectral range by long-lived greenhouse gases other than $CO_2$.

[67] For cooling rates, the strongest cooling rate change in the stratosphere is associated with $CO_2$ increase (case B) and ozone depletion (case H). Figure 15 (bottom) reports the cooling rate profiles and the biases with respect to AER for case L minus case A (i.e., a combined effect of all LLGHG change and 10% ozone depletion). Due to combined 10% ozone depletion and LLGHG changes, an increased cooling rate of about 0.25 K/d with respect to the reference case A is found at 1 hPa for AER (Figure 15). The model responses deviate between 2% (AMTRAC3) and 40% (UMSLIMCAT and UMUKCA-Leeds) from this value. The FLBLM deviation is about 3% at this level.

[68] Analyses of heating rate changes for individual cases (not shown) revealed additional understanding.

[69] 1. The maximum cooling rate bias with respect to AER for imposed $CO_2$ increase at 70 hPa is found for CCSRNIES. This value is more than a factor of four larger than the LBL bias. Also E39CA, MRI and SOCOL cooling rate biases are more than twice as large as LBL bias. UMUKCA-METO, UMUKCA-UCAM and UKMO-HADGEM3 underestimate the cooling rates by the same factor at this level. At 15 hPa, most of the models tend to underestimate cooling rates due to imposed $CO_2$ increase, with the maximum bias found for SOCOL and E39CA, except CCSRNIES and GEOSCCM which are too sensitive to $CO_2$ emission by a factor of 5. At 2 hPa, EMAC, ECHAM5 and LMDZ-new present the largest negative biases in the cooling rates, underestimating the effect of $CO_2$ increase. These biases are of the same order of magnitude as the biases for the same models in the heating rates found for a reduction in stratospheric ozone (case H).

[70] 2. With respect to AER the majority of the CCMVal models and other LBL models underestimate the cooling rate decrease associated with stratospheric ozone decrease at 70 hPa and 15 hPa whereas about half of the models overestimate it at 2 hPa.

[71] 3. CCSRNIES significantly overestimates the cooling rate associated with stratospheric $H_2O$ increase at 70 hPa and 15 hPa, followed by UMUKCA-METO, UMUKCA-UCAM and the two UKMO models at 70 hPa and by E39CA and SOCOL at 15 hPa, whereas LMDZrepro is not sensitive enough to $H_2O$ change at 15 hPa. CCSRNIES and the UKMO/UMUKCA based models also report too high sensitivity to $H_2O$ change in the upper stratosphere.

[72] A summary of heating and cooling rates biases by model is presented below. Only biases larger than the largest LBL bias are discussed.

#### 4.5.1. Heating Rates

[73] EMAC slightly overestimates the heating rate in the upper stratosphere. This is consistent with an overestimation of the ozone absorption at 2 hPa.

[74] CCSRNIES underestimates heating rate severely at 70 hPa, while it overestimates it at 2 hPa (~4%), which is consistent with an overestimation of absorption of solar radiation by ozone. This model is also too sensitive to the absorption of solar radiation by $H_2O$ at 15 hPa and 2 hPa in the infrared spectral region.

[75] GEOSCCM overestimates heating rates at 70 hPa and 2 hPa. At 70 hPa this is consistent with an overestimation of absorption of solar radiation by ozone.

[76] AMTRAC3, ECHAM5, LMDZ-new, CMAM, UMUKCA-UCAM, UMUKCA-HADGEM3 and the two UKMO models overestimate the heating rate at 2 hPa, consistent with too large sensitivity to absorption of solar radiation by ozone. All these models, except AMTRAC3 and

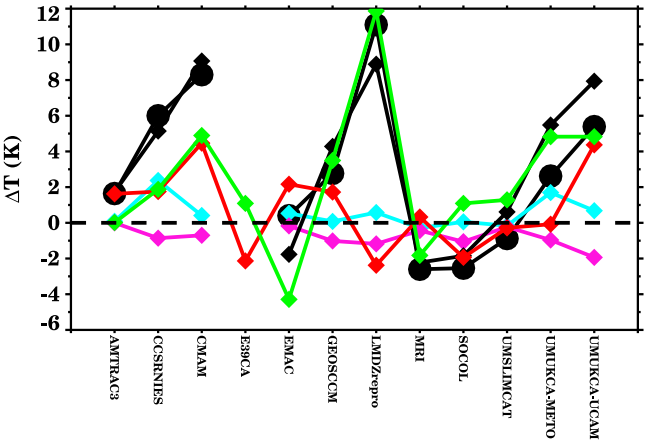


**Figure 16.** The bias in the simulated global mean temperature at 2 hPa from section 3 (black circles) and the estimated contributions of CCM biases in: ozone climatology (pink diamonds), water vapor climatology (light blue diamonds), and longwave/shortwave heating rates calculations (green/red diamonds). The total CCM bias (climatology and heating rate) is represented by black diamonds. See text for details.

UMUKCA-UCAM, are not sensitive enough to absorption of solar radiation by $H_2O$ in the infrared at 70 and 15 hPa.

[77] E39CA, LMDZrepro and SOCOL underestimate the heating rate at 2 hPa (~3%), consistent with an underestimation of $CO_2$ absorption.

[78] In general, almost all the models tend to overestimate the weak absorption of solar radiation by $CO_2$ in the lower and middle stratosphere, consistent with the results in section 4.4.

#### 4.5.2. Cooling Rates

[79] CCSRNIES overestimates the cooling rate in the lower stratosphere by ~50%. This is consistent with a too high sensitivity to the emission from $CO_2$ and also to $H_2O$.

[80] UMSLIMCAT and AMTRAC3 underestimate the cooling rate in the lower and middle stratosphere by around ~20% and ~15%, respectively. At 15 hPa there is a competing effect of too small a cooling from the emission of $CO_2$ and a too high cooling from the emission by $O_3$ and $H_2O$.

[81] UMUKCA-METO, UMUKCA-UCAM, UKMO-HADGEM3 and UKMO-Leeds underestimate the cooling rate in the lower stratosphere by ~15%. For the first three models, this underestimation is consistent with a too small sensitivity to $CO_2$ emission. All four models tend to be too sensitive to both $O_3$ and $H_2O$ emission.

[82] LMDZrepro underestimates the cooling rate at 70 hPa by ~10% and at 2 hPa by ~17%, showing a too small cooling from the emission of $O_3$, and from $H_2O$ emission at 2 hPa and a too large cooling from $CO_2$ emission at 2 hPa and $O_3$ emission in the lower stratosphere.

[83] CMAM underestimates the cooling rate in the lower stratosphere by ~13%. The model biases show an overestimated sensitivity to $O_3$ emission.

[84] SOCOL and E39CA underestimate the cooling rate in the middle stratosphere by ~10%. At 15 hPa they report a too small cooling for $CO_2$ and $H_2O$ emission and a too high cooling from $O_3$ emission.

[85] The EMAC cooling rate response to $CO_2$ increase (case B) substantially deviates from the LBL model results above 10 hPa. The same behavior is also observed for ECHAM5 and LMDZ-new models which exploit similar LW codes.

### 4.6. Radiation Scheme Errors and Model Temperature Biases

[86] In this section the assessment of the heating and cooling rates from section 4 is applied to the analysis of the stratospheric temperature biases simulated by the CCMs. Biases in the global mean temperature climatology (reported in section 3.1) are compared with the temperature errors arising both from the inaccuracy of the radiative heating rate calculations and from the biases in simulated ozone and water vapor mixing ratios (see section 3.1).

[87] The potential errors in the temperature simulations from errors in heating and cooling rates are estimated by converting the results from the off-line heating and cooling rate calculations for reference case A to temperature using precalculated relaxation times. Relaxation times represent the thermal inertia due to radiative transfer and are estimated from the cooling rate response to a constant (with height) 1 K temperature change using the correlated k-distribution scheme by *Li and Barker* [2005]. At three considered levels in the lower (70 hPa), middle (15 hPa) and upper (2 hPa) stratosphere, the estimated global mean relaxation times are 180, 25 and 8 days, respectively.

[88] The contribution from the ozone and water vapor biases is estimated using biases from section 3.1 to scale the radiative response to the stratospheric ozone depletion and water vapor increase (cases H and J) simulated by the participating models. The obtained errors in the heating and cooling rates associated with the model's ozone and water vapor biases are also converted to an equivalent temperature bias using the relaxation time. This procedure provides temperature errors for all participating models related both to the errors in the LW and SW radiation codes and to the errors in the simulated ozone and water vapor fields.

[89] The analysis has been carried out for the upper, middle and lower stratosphere (pressure levels 2, 15 and 70 hPa) and the conclusions drawn in this section generally confirm the qualitative assessment of the upper stratospheric model performance in section 3.1. The results for the upper stratosphere (2 hPa) are shown in Figure 16. At this level the total temperature errors derived from the inaccuracy of the radiation schemes and the biases in ozone and water vapor abundances are very close to the temperature biases simulated by the CCMs for most of the participating models (black diamonds and black circles, respectively). For AMTRAC3 the small positive temperature bias is explained by overestimated solar heating rates. The large temperature bias for CCSRNIES results from underestimated longwave cooling rates, overestimated solar heating rates, and a negative bias in the simulated water vapor mixing ratio, with all three factors contributing about equally. The large warm bias for CMAM is explained both by overestimation of solar heating rates and underestimation of cooling rates. The small temperature bias for EMAC is due to its overestimated cooling rates, which is partly compensated by SW heating rates and the simulated water vapor mixing ratio. For GEOSCCM the warm bias is produced by overestimated

heating rates and underestimated cooling rates and is partially compensated by underestimated ozone mixing ratios. The very large temperature bias for LMDZrepro is dominated by a massive underestimation of the cooling rates. The negative temperature bias for MRI is mainly due to slightly overestimated cooling rates, while the same sized bias in SOCOL is primarily due to underestimated solar heating rates and a negative bias in the ozone mixing ratio. UMSLIMCAT has only a very small cold bias, for which a small underestimation of the cooling rates is compensated by the cumulative effects of small errors in solar heating and water vapor and ozone mixing ratios. Warm biases in UMUKCA-METO and UMUKCA-UCAM result primarily from underestimated cooling rates, although underestimated water vapor mixing ratios for UMUKCA-METO and overestimated solar heating rates and compensated underestimated ozone mixing ratios for UMUKCA-UCAM also contribute significantly.

[90] Four models were singled out in the analysis of simulated temperature climatologies in section 3.1 as likely to have deficiencies in their radiation schemes in the upper stratosphere: CCSRNIES, CMAM, CNRM-ACM and LMDZrepro. While CNRM-ACM is not analyzed here, the present analysis confirms the qualitative assessment made in section 3.1 for the other three models.

[91] In the middle stratosphere (15 hPa) and in the lower stratosphere (70 hPa) the temperature biases and estimated errors (not shown) are generally well correlated but significant discrepancies between the two values exist, making a similar analysis less useful for these heights. This is probably due to a number of reasons. First, using relaxation time for the conversion of heating rate to temperature is a rough approach which works better in the vicinity of the stratopause than in the middle and lower stratosphere where the relaxation time depends more strongly on the shape of the perturbation and has a strong latitudinal dependence. Second, the effect of errors in $O_3$ and $H_2O$ mixing ratios has been estimated based on the local biases. However, nonlocality plays an important role in the middle and lower stratosphere for both solar heating and longwave cooling rate calculations. Third, the temperature biases reported in section 3.1 are based on the annually averaged global mean climatology, whereas heating rates used to estimate errors are global values based on calculations at five latitudes for January conditions. And finally, the effect of clouds and volcanic aerosol, which is important in the lower and middle stratosphere, was not evaluated in the framework of this exercise.

## 5. Solar Signal in CCMs

[92] The incident solar radiation at the top of Earth's atmosphere varies on different time scales. Observational studies [e.g., *Randel et al.*, 2009] found a statistical significant decadal signal in annual mean upper stratospheric temperature of up to 1 K, associated with the 11 year solar activity cycle. While the total solar irradiance (TSI), i.e., the spectrally integrated solar irradiance at the top of Earth's atmosphere, varies only by about 0.1% over the 11 year cycle, larger variations occur in the ultraviolet (UV) part of the spectrum, reaching several percent in the ozone absorption bands that are responsible for the SW heating of the stratosphere. However, given the much lower intensity in the UV spectral region compared to the visible (VIS) and near-infrared (IR) parts of the solar spectrum and because of the historical focus of numerical global modeling on the troposphere where absorption of solar UV radiation by ozone plays only a very minor role, SW radiation codes in GCMs and CCMs do not consider the solar irradiance for the wavelengths shorter than ~250 nm and quite often exploit broadband parameterizations using TSI as input variable. Depending on the radiation scheme, fractions of TSI are then used to calculate solar fluxes and heating rates in one or two SW absorption bands from the top of the atmosphere to the surface. More sophisticated SW radiation codes designed for applications to the middle atmosphere usually consider extended spectral range and include more spectral bands in the UV/VIS. *Egorova et al.* [2004] and *Nissen et al.* [2007] compared the performance of SW radiation codes with different spectral resolution and showed that the observed solar temperature signal in the stratosphere can only be reproduced in models that allow for the effects of spectral variations between solar minimum and maximum.

[93] In this section we will address the following questions. (1) How sensitive are the CCM SW radiation codes to changes in solar irradiance and ozone? (2) How well is the 11 year radiative solar signature reproduced by the participating SW radiation codes in comparison with reference LBL codes?

### 5.1. Experimental Setup

[94] Heating rate differences between the minimum and maximum phases of the 11 year solar cycle have been calculated in stand-alone versions of the CCM shortwave radiation parameterizations and in line-by-line (LBL) models for prescribed spectral flux and solar induced ozone differences between the minimum and maximum phases of the 11 year solar cycle.

[95] The spectral solar irradiance (SSI) and TSI data to be used in this comparison are based on the method described by *Lean et al.* [2005]. Extraterrestrial spectral solar irradiance for the spectral range 120–100,000 nm were provided with a spectral resolution ranging from 1 to 50 nm as well as the spectral integral over all wavelengths, i.e., TSI. The monthly mean solar irradiance of September 1986 and November 1989 has been selected for solar minimum and solar maximum conditions, respectively. For mean solar conditions average data were derived from the period 1950 to 2006. Depending on the individual SW radiation codes the modeling groups were requested to either use the suggested TSI for solar minimum and maximum conditions, or to integrate the provided high-resolution spectral irradiances to match the broader spectral intervals of their own SW radiation codes and to adapt the total solar irradiance to be consistent with the integral over all intervals. To study the effect of solar induced ozone variations on heating rates, experiments with mean solar irradiance and prescribed ozone changes between solar minimum and maximum were carried out. The ozone changes have been derived from two-dimensional, photochemical model calculations [*Haigh*, 1994] to ensure smooth distributions of the changes. Other settings of the experiments were identical to the 1980 con-

**Table 5.** Experimental Setup for Off-Line Solar Variability Simulations

| Experiment | Solar Irradiance | Ozone |
|---|---|---|
| A | mean | 1980 climatology |
| O | maximum | 1980 climatology |
| P | minimum | 1980 climatology |
| R | mean | maximum |
| S | mean | minimum |

trol simulation (case A, Table 3). Table 5 gives an overview of the experiments.

[96] The participating CCM SW radiation codes and the provided SW radiative heating rates are summarized in Table 6 which also indicates whether the radiation codes are forced with TSI or spectral irradiance data. The results of these off-line calculations have been evaluated against reference calculations from the LBL radiation code LibRadtran [*Mayer and Kylling*, 2005].

### 5.2. Sensitivity of the Solar Signal to Spectral Resolution

[97] Figure 17 shows global mean profiles of the differences in SW heating rates between solar minimum and maximum in January. In Figure 17 (left) only solar irradiance variations are taken into account, and in Figure 17 (middle) the effects of prescribed solar induced ozone changes only. Figure 17 (right) shows the total effects of solar irradiance and prescribed solar induced ozone changes between solar minimum and maximum. The largest response to 11 year solar irradiance changes (experiments O-P (Figure 17, left)) occurs in the stratopause region with global mean heating rate changes from solar minimum to maximum of about 0.12 K/d in the LibRadtran reference model (black line). The results of the CCM radiation schemes can be grouped into three categories: (1) schemes that closely follow the reference heating rate change profile, i.e., CMAM, EMAC and CCSRNIES, and with some minor deviations SOCOL, (2) two schemes that reproduce about half of the reference heating rate differences (ECHAM5 and UMSLIMCAT) and (3) schemes that have an almost negligible radiative response to solar irradiance changes of less 0.02 K/d, like ECHAM4, LMDZrepro, UMUKCA-METO, and UMUKCA-UCAM.

[98] Differences between the three groups can be explained by the spectral resolution of the prescribed solar irradiance change between solar minimum and maximum. With 44 spectral intervals between 121 and 683 nm the EMAC scheme reproduces the reference profile over the whole stratosphere very well; similarly the CMAM code with 8 bands between 121 and 305.5 nm and only 3 bands for ozone absorption between 206 and 305.5 nm. SOCOL (4 spectral intervals between 120 and 680 nm) overestimates the maximum SW heating rate difference in the lower mesosphere by about 10%, associated with an underestimation in the lower stratosphere. In contrast, the SW radiation codes in LMDZrepro, UMUKCA-METO, UMUKCA-UCAM, and ECHAM4 that are driven by TSI changes between solar minimum and maximum only, are not able to capture the magnitude of the SW heating rate changes between solar minimum and maximum.

[99] The SW radiation scheme of the Unified Model (UM) model series can also be driven by spectral irradiance changes, as was done for example in the REF-B1 simulation of UMSLIMCAT. This allows for a direct assessment of the effect of spectral irradiance versus TSI input data. As seen in Figure 17 (left), the SW heating rate response of the spectrally forced off-line calculation with UMSLIMCAT is stronger than in the TSI forced UMUKCA-METO and UMUKCA–UCAM models. However, with a SW heating rate difference of ~0.07 K/d, UMSLIMCAT reproduces only about 50% of the LBL model result. A similar result as for UMSLIMCAT is obtained for ECHAM5. The ECHAM5 off-line radiation code was included into this comparison to investigate the effect of adding two bands in the UV to the single UV/VIS absorption band used in the ECHAM4 code [*Cagnazzo et al.*, 2007]. Although with the additional absorption bands (185–690 nm) the full spectral range of ozone absorption is resolved, only 50% of the heating rate differences between solar minimum and maximum can be simulated.

[100] The global mean SW heating rate response to prescribed solar induced ozone changes (experiments R-S (Figure 17, middle)) in the reference model reaches about 0.07 K/d from solar minimum to maximum, that is approximately 65% of the response to the solar irradiance variations. The strongest response occurs in the upper stratosphere, about 10 km lower than the strongest response to irradiance changes. This behavior is qualitatively well reproduced by the different CCM radiation codes. Deviations from the LBL code are much smaller than for the irradiance changes, as mean solar irradiance was prescribed to isolate the clean 'ozone effect.' Differences between the models occur due to the band width adopted and generally correspond to the differences encountered in case A. Note that the 'ozone effect' exceeds the effect of solar irradiance variations below 10 hPa emphasizing the importance of considering the feedback of changes in ozone photochemistry during a solar cycle on the SW radiation budget.

[101] The total SW heating rate change between solar minimum and maximum, i.e., due to both solar irradiance changes and the solar induced ozone changes (Figure 17, right), clearly illustrates that those CCM SW radiation codes that use only TSI variations underestimate the solar radiative signal by about 50% in terms of heating rates.

[102] The response to solar variability obtained with the CCM SW radiation codes in off-line mode is generally consistent with the solar response in the transient REF-B1

**Table 6.** Participating Off-Line SW Radiation Codes and Ways of Prescribing Solar Variability

| CCM | Total Solar Irradiance | Spectral |
|---|---|---|
| CCSRNIES | No | Yes |
| CMAM | No | Yes |
| ECHAM4 | Yes | No |
| ECHAM5 | No | Yes |
| EMAC | No | Yes |
| LMDZrepro | Yes | No |
| SOCOL | No | Yes |
| UMSLIMCAT | No | Yes |
| UMUKCA-METO | Yes | No |
| UMUKCA-UCAM | Yes | No |

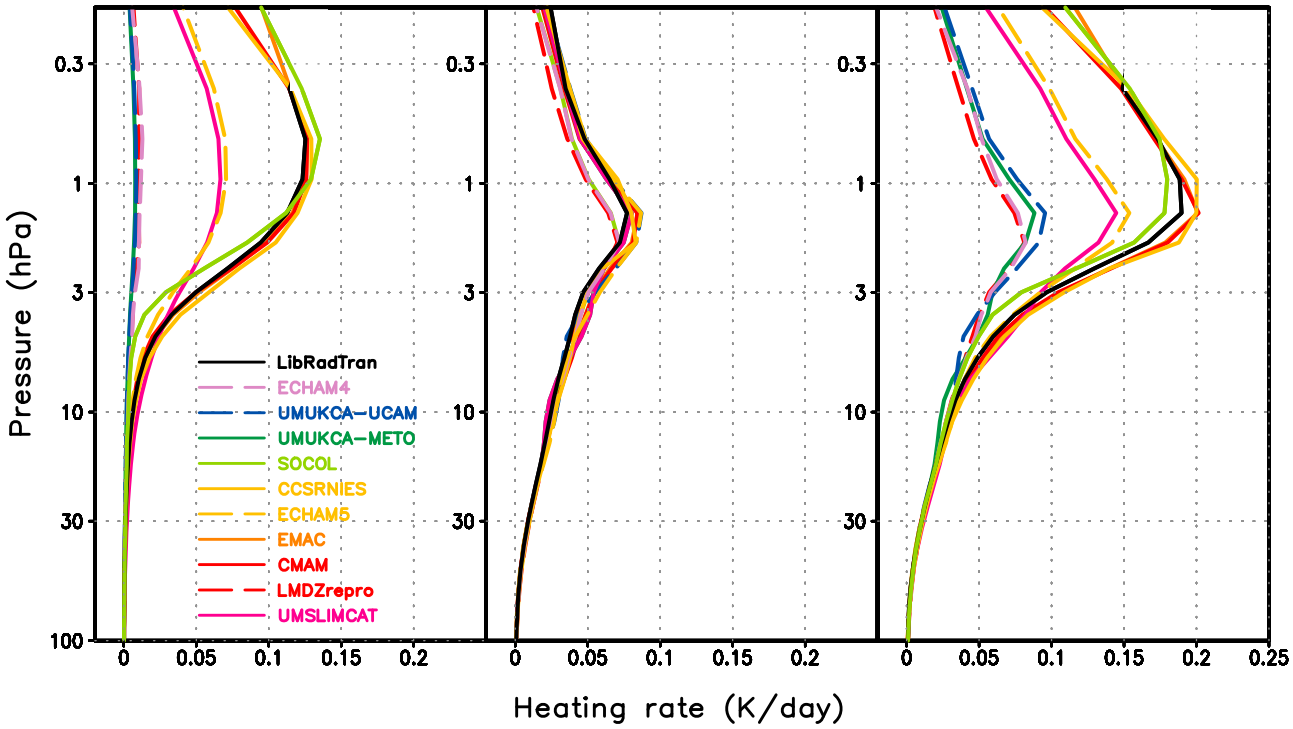


**Figure 17.** Global mean, shortwave heating rate differences between minimum and maximum of the 11 year solar cycle in January (K/d), calculated off-line in CCM radiation schemes and one reference LBL model. (left) Radiative response to prescribed solar irradiance change (experiments O-P, Table 5), (middle) radiative response to solar induced ozone change (experiments R-S, Table 5), and (right) total radiative response (experiments (O-P) + (R-S), Table 5).

simulations [see *SPARC CCMVal*, 2010] The REF-B1 solar heating rate differences for those models, which also provided off-line heating rates (CCSRNIES, CMAM, EMAC, and LMDZrepro) range between 0.07 and 0.17 K per day per 100 units of the F10.7cm solar flux around the tropical stratopause [*SPARC CCMVal*, 2010, Figure 8.12]. By multiplying these values by a factor 1.3 to allow for the transient response we obtain an estimate of the SW heating rate differences between solar minimum and maximum that can be compared with the off-line calculations. There is good agreement between online and off-line calculated heating rate differences for the four CCMs (not shown). For example, we find an annual mean tropical heating rate difference of 0.20 K per day in the REF-B1 run of CMAM and a heating rate difference of 0.22 K per day at the Equator in January from the CMAM off-line code.

[103] In chapter 8 of the SPARC CCMVal report, the temperature response to decadal solar forcing in the CCMs was derived by a multiple linear regression analysis [*SPARC CCMVal*, 2010, Figure 8.11]. The strongest solar temperature signal is found consistently in the tropical upper stratosphere/lower mesosphere, indicating that the direct mechanism of heating by absorption of enhanced UV radiation at solar maximum is well captured by the spectrally resolving SW radiation schemes. The reduced decadal temperature signal in LMDZrepro can be explained by the underestimation of the spectral solar forcing that was identified in the off-line calculations. However, while the responses to solar irradiance changes in the spectrally resolving radiation codes of CCSRNIES, CMAM, EMAC, and SOCOL are close to each other (Figure 17, left), the solar temperature responses in the corresponding REF-B1 simulations of these models show a considerable spread in the upper stratosphere and mesosphere [*SPARC CCMVal*, 2010, Figure 8.11a], which cannot be explained by a direct radiative effect alone. Similarly, indirect dynamical processes seem to contribute to the strong solar response of mesospheric temperature in the UMSLIMCAT REF-B1 simulation, as the off-line calculation shows that its SW radiation code underestimates the heating rate response to UV variations.

## 6. Summary

[104] The work in this paper has shown that CCM global mean stratospheric temperatures and their change can give an indication of errors in radiative transfer codes and/or atmospheric composition. Biases in the global temperature climatology are generally small, although five out of 18 CCMs show biases in their climatology that likely indicate problems with their radiative transfer codes. Temperature trends also generally agree well with observations, although one model shows significant discrepancies that appear to be due to radiation errors. Heating rates and estimated temperature changes from $CO_2$, ozone and water vapor changes are generally well modeled. Other gases ($N_2O$, $CH_4$, CFCs) have only played a minor role in stratospheric temperature change but their heating rates are estimated with large

fractional errors in many models. Models that do not account for variations in the spectrum of solar irradiance but only consider changes in total (spectrally integrated) solar irradiance (TSI) cannot properly simulate solar-induced variations in stratospheric temperature. The combined long-lived greenhouse gas global annual mean instantaneous net radiative forcing at the tropopause is within 30% of line-by-line models for all CCM radiation codes tested. Problems remain simulating radiative forcing for stratospheric water vapor and ozone changes with a range of errors between 3% and 200% compared to line by line models and even large deviations among the LBL models themselves.

[105] Performing a comparison of radiation schemes has been challenging. This work would have benefited from more CCM radiation schemes being run independently of their host models. We suggest that in the future radiation schemes should regularly be involved in comparison exercises based on detailed sets of reference calculations from line-by-line models. Ideally, solar and longwave schemes should be evaluated for a range of realistic circumstances. Future radiation scheme comparisons should also ideally evaluate the radiative effects of aerosols and clouds as well as trace gases. They should also evaluate the effect of approximations made in CCMs, such as the frequency of radiative transfer calculations and the effects of plane-parallel/sphericity approximations. Photolysis and solar heating calculations should be merged for consistency. Non local thermodynamic equilibrium effects should be accounted for above 70 km to correctly simulate heating and cooling rates in this region. CCMs should include spectral variations in solar irradiance when modeling solar variability in order to induce the correct stratospheric temperature change. Further work is needed to assess the level of spectral detail required.

## References


Andrews, D. G., J. R. Holton, and C. B. Leovy (1987), *Middle Atmosphere Dynamics*, 489 pp., Academic., San Diego, Calif.

Austin, J., et al. (2009), Coupled chemistry climate model simulations of stratospheric temperatures and their trends for the recent past, *Geophys. Res. Lett.*, *36*, L13809, doi:10.1029/2009GL038462.

Barker, H. W., et al. (2003), Assessing 1D atmospheric solar radiative transfer models: Interpretation and handling of unresolved clouds, *J. Clim.*, *16*, 2676–2699, doi:10.1175/1520-0442(2003)016<2676:ADASRT>2.0.CO;2.

Brasseur, G. P., and S. Solomon (2005), *Aeronomy of the Middle Atmosphere*, 658 pp., Springer, New York.

Briegleb, B. P. (1992), Delta-Eddington approximation for solar-radiation in the NCAR Community Climate Model, *J. Geophys. Res.*, *97*, 7603–7612, doi:10.1029/92JD00291.

Cagnazzo, C., E. Manzini, M. A. Giorgetta, P. M. D. Forster, and J. J. Morcrette (2007), Impact of an improved shortwave radiation scheme in the MAECHAM5 General Circulation Model, *Atmos. Chem. Phys.*, *7*(10), 2503–2515, doi:10.5194/acp-7-2503-2007.

Chou, M.-D., and M. J. Suarez (1999), A solar radiation parameterization for Atmospheric studies, *NASA Tech. Rep. 104606*, vol. 15, 40 pp., NASA Goddard Space Flight Cent., Greenbelt, Md.

Chou, M.-D., M. J. Suarez, C.-H. Ho, M. M.-H. Yan, and K.-T. Lee (1998), Parameterizations for cloud overlapping and short-wave single-scattering properties for use in general circulation and cloud ensemble members, *J. Clim.*, *11*, 202–214, doi:10.1175/1520-0442(1998)011<0202:PFCOAS>2.0.CO;2.

Chou, M.-D., M. J. Suarez, X. Z. Liang, and M. M.-H. Yan (2001), A thermal infrared radiations parameterization for atmospheric studies, *NASA Tech. Rep. 104606*, vol. 19, 56 pp., NASA Goddard Space Flight Cent., Greenbelt, Md.

Clough, S. A., and M. J. Iacono (1995), Line-by-line calculations of atmospheric fluxes and cooling rates. II: Application to carbon dioxide, ozone, methane, nitrous oxide, and the halocarbons, *J. Geophys. Res.*, *100*, 16,519–16,535, doi:10.1029/95JD01386.

Clough, S. A., M. W. Shephard, E. J. Mlawer, J. S. Delamere, M. J. Iacono, K. Cady-Pereira, S. Boukabara, and P. D. Brown (2005), Atmospheric radiative transfer modeling: A summary of the AER codes: Short communication, *J. Quant. Spectrosc. Radiat. Transfer*, *91*, 233–244, doi:10.1016/j.jqsrt.2004.05.058.

Collins, W. D., et al. (2004), Description of the NCAR community atmosphere model (CAM3.0), *Tech. Rep. NCAR/TN-464+STR*, Natl. Cent. for Atmos. Res., Boulder, Colo.

Collins, W. D., et al. (2006), Radiative forcing by well-mixed greenhouse gases: Estimates from climate models in the Intergovernmental Panel on Climate Change (IPCC) Fourth Assessment Report (AR4), *J. Geophys. Res.*, *111*, D14317, doi:10.1029/2005JD006713.

Edwards, J. M., and A. Slingo (1996), Studies with a flexible new radiation code. I: Choosing a configuration for a large scale model, *Q. J. R. Meteorol. Soc.*, *122*, 689–719, doi:10.1002/qj.49712253107.

Egorova, T., E. Rozanov, E. Manzini, M. Haberreiter, W. Schmutz, V. Zubov, and T. Peter (2004), Chemical and dynamical response to the 11-year variability of the solar irradiance simulated with a chemistry-climate model, *Geophys. Res. Lett.*, *31*, L06119, doi:10.1029/2003GL019294.

Ellingson, R. G., S. J. Ellis, and S. B. Fels (1991), The intercomparison of radiation codes used in climate models: Long-wave results, *J. Geophys. Res.*, *96*, 8929–8953, doi:10.1029/90JD01450.

Feigelson, E. M., and L. R. Dmitrieva (Eds.) (1983), Radiative algorithms in the atmospheric general circulation models: A review, *Rep. All-Union Res. Hydrometeorol. Inst. Issue 1*, 43 pp., Hydrometeoizdat, Moscow.

Fels, S. B. (1985), Radiative dynamical interactions in the middle atmosphere, *Adv. Geophys.*, *28*, 277–300, doi:10.1016/S0065-2687(08)60227-7.

Fomichev, V. I. (2009), The radiative energy budget of the middle atmosphere and its parameterizations in general circulation models, *J. Atmos. Sol. Terr. Phys.*, *71*, 1577–1585, doi:10.1016/j.jastp.2009.04.007.

Fomichev, V. I., and G. M. Shved (1994), On the closeness of the middle atmosphere to the state of radiative equilibrium: An estimation of net dynamical heating, *J. Atmos. Terr. Phys.*, *56*, 479–485, doi:10.1016/0021-9169(94)90196-1.

Fomichev, V. I., J.-P. Blanchet, and D. S. Turner (1998), Matrix parameterization of the 15 $\mu$m $CO_2$ band cooling in the middle and upper atmosphere for variable $CO_2$ concentration, *J. Geophys. Res.*, *103*, 11,505–11,528, doi:10.1029/98JD00799.

Fomichev, V. I., C. Fu, J. de Grandpré, S. R. Beagley, V. P. Ogibalov, and J. C. McConnell (2004), Model thermal response to minor radiative energy sources and sinks in the middle atmosphere, *J. Geophys. Res.*, *109*, D19107, doi:10.1029/2004JD004892.

Fomin, B. A. (2006), Monte-Carlo algorithm for line-by-line calculations of thermal radiation in multiple scattering layered atmospheres, *J. Quant. Spectrosc. Radiat. Transfer*, *98*, 107–115, doi:10.1016/j.jqsrt.2005.05.078.

Fomin, B. A., and I. P. Mazin (1998), Model for an investigation of radiative transfer in cloudy atmosphere, *Atmos. Res.*, *47–48*, 127–153, doi:10.1016/S0169-8095(98)00056-8.

Forster, P. M. D., M. Ponater, and W. Y. Zhong (2001), Testing broadband radiation schemes for their ability to calculate the radiative forcing and temperature response to stratospheric water vapour and ozone changes, *Meteorol. Z.*, *10*, 387–393, doi:10.1127/0941-2948/2001/0010-0387.

Forster, P., et al. (2007), Changes in atmospheric constituents and in radiative forcing, in *Climate Change 2007: The Physical Science Basis. Contribution of Working Group I to the Fourth Assessment Report of the Intergovernmental Panel on Climate Change*, edited by S. Solomon et al., pp. 129–234, Cambridge Univ. Press, Cambridge, U. K.

Fouquart, Y., and B. Bonnel (1980), Computations of solar heating of the Earth's atmosphere: A new parameterization, *Beitr. Phys. Atmos.*, *53*, 35–62.

Fouquart, Y., B. Bonnel, and V. Ramaswamy (1991), Intercomparing shortwave radiation codes for climate studies, *J. Geophys. Res.*, *96*, 8955–8968, doi:10.1029/90JD00290.

Goldblatt, C., T. M. Lenton, and A. J. Watson (2009), An evaluation of the long-wave radiative transfer code used in the Met Office Unified Model, *Q. J. R. Meteorol. Soc.*, *135*, 619–633, doi:10.1002/qj.403.

Haigh, J. D. (1994), The role of stratospheric ozone in modulating the solar radiative forcing of climate, *Nature*, *370*, 544–546, doi:10.1038/370544a0.

Halthore, R. N., et al. (2005), Intercomparison of shortwave radiative transfer codes and measurements, *J. Geophys. Res.*, *110*, D11206, doi:10.1029/2004JD005293.

Jonsson, A. I., V. I. Fomichev, and T. G. Shepherd (2009), The effect of nonlinearity in $CO_2$ heating rates on the attribution of stratospheric ozone and temperature changes, *Atmos. Chem. Phys.*, *9*, 8447–8452, doi:10.5194/acp-9-8447-2009.

Kockarts, G. (1980), Nitric oxide cooling in the terrestrial thermosphere, *Geophys. Res. Lett.*, *7*, 137–140, doi:10.1029/GL007i002p00137.

Lacis, A. A., and J. E. Hansen (1974), A parameterization for the absorption of solar radiation in the Earth's atmosphere, *J. Atmos. Sci.*, *31*, 118–133, doi:10.1175/1520-0469(1974)031<0118:APFTAO>2.0.CO;2.

Lacis, A., J. E. Hansen, and M. Sato (1992), Climate forcing by stratospheric aerosols, *Geophys. Res. Lett.*, *19*, 1607–1610, doi:10.1029/92GL01620.

Lean, J. L., G. Rottman, J. Harder, and G. Kopp (2005), SORCE contributions to new understanding of global change and solar variability, *Sol. Phys.*, *230*, 27–53, doi:10.1007/s11207-005-1527-2.

Li, J., and H. W. Barker (2005), A radiation algorithm with correlated-k distribution. Part I: Local thermal equilibrium, *J. Atmos. Sci.*, *62*, 286–309, doi:10.1175/JAS-3396.1.

London, J. (1980), Radiative energy sources and sinks in the stratosphere and mesosphere, in *Proceedings of the NATO Advanced Institute on Atmospheric Ozone*, edited by A. C. Aikin, p. 703, U.S. Dep. of Transport., Washington, D. C.

Luther, F. M., R. G. Ellingson, Y. Fouquart, S. Fels, N. A. Scott, and W. J. Wiscombe (1988), Intercomparison of radiation codes in climate models (ICRCCM)—Longwave clear-sky results—A workshop summary, *Bull. Am. Meteorol. Soc.*, *69*, 40–48.

Marsh, D. R., R. R. Garcia, D. E. Kinnison, B. A. Boville, S. Walters, K. Matthes, and S. C. Solomon (2007), Modeling the whole atmosphere response to solar cycle changes in radiative and geomagnetic forcing, *J. Geophys. Res.*, *112*, D23306, doi:10.1029/2006JD008306.

Mayer, B., and A. Kylling (2005), Technical note: The LibRadtran software package for radiative transfer calculations: Description and examples of use, *Atmos. Chem. Phys.*, *5*, 1855–1877, doi:10.5194/acp-5-1855-2005.

Mlawer, E. J., S. J. Taubman, P. D. Brown, M. J. Iacono, and S. A. Clough (1997), Radiative transfer for inhomogeneous atmospheres: RRTM, a validated correlated-k model for the longwave, *J. Geophys. Res.*, *102*, 16,663–16,682, doi:10.1029/97JD00237.

Morcrette, J.-J. (1990), Impact of changes to the radiation transfer parameterizations plus cloud optical properties in the ECMWF model, *Mon. Weather Rev.*, *118*, 847–873, doi:10.1175/1520-0493(1990)118<0847:IOCTTR>2.0.CO;2.

Morcrette, J.-J. (1991), Radiation and cloud radiative properties in the ECMWF operational weather forecast model, *J. Geophys. Res.*, *96*, 9121–9132, doi:10.1029/89JD01597.

Morgenstern, O., et al. (2010), Review of the formulation of present-generation stratospheric chemistry-climate models and associated external forcings, *J. Geophys. Res.*, *115*, D00M02, doi:10.1029/2009JD013728.

Myhre, G., and F. Stordal (1997), Role of spatial and temporal variations in the computation of radiative forcing and GWP, *J. Geophys. Res.*, *102*, 11,181–11,200, doi:10.1029/97JD00148.

Myhre, G., and F. Stordal (2001), On the tradeoff of the thermal and solar radiative impact of contrails, *Geophys. Res. Lett.*, *28*, 3119–3122, doi:10.1029/2001GL013193.

Myhre, G., F. Stordal, I. Gausemel, C. Nielsen, and E. Mahieu (2006), Line-by-line calculations of thermal infrared radiation representative for global condition: CFC-12 as an example, *J. Quant. Spectrosc. Radiat. Transfer*, *97*, 317–331, doi:10.1016/j.jqsrt.2005.04.015.

Myhre, G., et al. (2009), Intercomparison of radiative forcing of stratospheric water vapour and contrails, *Meteorol. Z.*, *18*, 585–596, doi:10.1127/0941-2948/2009/0411.

Nakajima, T., and M. Tanaka (1986), Matrix formulation for the transfer of solar radiation in a plane-parallel scattering atmosphere, *J. Quant. Spectrosc. Radiat. Transfer*, *35*, 13–21, doi:10.1016/0022-4073(86)90088-9.

Nakajima, T., M. Tsukamoto, Y. Tsuhima, A. Numaguti, and T. Kimura (2000), Modeling of the radiative process in an atmospheric general circulation model, *Appl. Opt.*, *39*, 4869–4878, doi:10.1364/AO.39.004869.

Nissen, K., K. Matthes, U. Langematz, and B. Mayer (2007), Towards a better representation of the solar cycle in general circulation models, *Atmos. Chem. Phys.*, *7*, 5391–5400, doi:10.5194/acp-7-5391-2007.

Ogibalov, V. P., and V. I. Fomichev (2003), Parameterization of solar heating by the near IR $CO_2$ bands in the mesosphere, *Adv. Space Res.*, *32*, 759–764, doi:10.1016/S0273-1177(03)80069-8.

Pitari, G. (1993), A numerical study of the possible perturbation of stratospheric dynamics due to Pinatubo aerosols: Implications for tracer transport, *J. Atmos. Sci.*, *50*, 2443–2461, doi:10.1175/1520-0469(1993)050<2443:ANSOTP>2.0.CO;2.

Pitari, G., E. Mancini, V. Rizi, and D. T. Shindell (2002), Impact of future climate and emission changes on stratospheric aerosols and ozone, *J. Atmos. Sci.*, *59*, 414–440, doi:10.1175/1520-0469(2002)059<0414:IOFCAE>2.0.CO;2.

Portmann, R., S. Solomon, J. Fishman, J. R. Olson, J. T. Kiehl, and B. Briegleb (1997), Radiative forcing of the Earth's climate system due to tropical tropospheric ozone production, *J. Geophys. Res.*, *102*, 9409–9417, doi:10.1029/96JD04007.

Randel, W. J., and F. Wu (2007), A stratospheric ozone profile data set for 1979–2005: Variability, trends, and comparisons with column ozone data, *J. Geophys. Res.*, *112*, D06313, doi:10.1029/2006JD007339.

Randel, W. J., et al. (2009), An update of observed stratospheric temperature trends, *J. Geophys. Res.*, *114*, D02107, doi:10.1029/2008JD010421.

Roeckner, E., et al. (2003), The atmospheric general circulation model ECHAM5. Part I: Model description, *MPI Rep. 218*, 90 pp., Max-Planck-Inst. für Meteorol., Hamburg, Germany.

Shibata, K., and T. Aoki (1989), An infrared radiative scheme for the numerical models of weather and climate, *J. Geophys. Res.*, *94*, 14,923–14,943, doi:10.1029/JD094iD12p14923.

Shibata, K., and A. Uchiyama (1994), An application of the discrete ordinate method to terrestrial radiation in climate models, *J. Atmos. Sci.*, *51*, 3531–3538, doi:10.1175/1520-0469(1994)051<3531:AAOTDO>2.0.CO;2.

Shine, K. P., et al. (2003), A comparison of model-simulated trends in stratospheric temperatures, *Q. J. R. Meteorol. Soc.*, *129*, 1565–1588, doi:10.1256/qj.02.186.

SPARC CCMVal (2010), SPARC Report on the Evaluation of Chemistry-Climate Models, edited by V. Eyring, T. G. Shepherd, and D. W. Waugh, *SPARC Rep. 5*, Univ. of Toronto, Toronto, Ont., Canada. (Available at http://www.atmosp.physics.utoronto.ca/SPARC.)

Sud, Y. C., W. C. Chao, and G. K. Walker (1993), Dependence of rainfall on vegetation: Theoretical consideration, simulation experiments, observations, and inferences from simulated atmospheric soundings, *J. Arid Environ.*, *25*, 5–18, doi:10.1006/jare.1993.1038.

Uppala, S., et al. (2005), The ERA-40 Re-Analysis, *Q. J. R. Meteorol. Soc.*, *131*, 2961–3012, doi:10.1256/qj.04.176.

World Meteorological Organization (2003), Scientific assessment of ozone depletion: 2002, *Tech. Rep. 47*, 498 pp., Geneva, Switzerland.

Zdunkowski, W. G., R. M. Welch, and G. Korb (1980), An investigation of the structure of typical two-stream-methods for the calculation of solar fluxes and heating rates in clouds, *Contrib. Atmos. Phys.*, *53*, 147–166.

Zhong, W., and J. D. Haigh (2001), An efficient and accurate correlated-k parameterization of infrared radiative transfer for troposphere-stratosphere-mesosphere GCMs, *Atmos. Sci. Lett.*, *1*, 125–135, doi:10.1006/asle.2000.0022.

Zhong, W., J. D. Haigh, D. Belmiloud, R. Schermaul, and J. Tennyson (2001), The impact of new water vapour spectral line parameters on the calculation of atmospheric absorption, *Q. J. R. Meteorol. Soc.*, *127*, 1615–1626, doi:10.1002/qj.49712757508.

Zhong, W., S. M. Osprey, L. J. Gray, and J. D. Haigh (2008), Influence of the prescribed solar spectrum on calculations of atmospheric temperature, *Geophys. Res. Lett.*, *35*, L22813, doi:10.1029/2008GL035993.

H. Akiyoshi, National Institute for Environmental Studies, Tsukuba 305-8506, Japan. (hakiyosi@nies.go.jp)

C. Cagnazzo, Centro Euro-Mediterraneo per i Cambiamenti Climatici, Viale Aldo Moro 44, I-40127, Bologna, Italy. (chiara.cagnazzo@cmcc.it)

V. Falaleeva, A.M. Obukhov Institute of Atmospheric Physics, Russian Academy of Sciences, Pyzhevskii per. 3, 119017 Moscow, Russia. (victory@ifaran.ru)

V. I. Fomichev, ESSE, York University, 4700 Keele St., Toronto, ON M3J 1P3, Canada. (victor@nimbus.yorku.ca)

B. Fomin, Central Aerological Observatory, Pervomayskaya Street 3, 141700 Moscow, Russia. (b.fomin@mail.ru)

P. Forster, School of Earth and Environment, University of Leeds, Leeds LS2 9JT, UK. (piers@env.leeds.ac.uk)

N. Gillett and J. Li, Canadian Centre for Climate Modelling and Analysis, University of Victoria, PO Box 1700, STN CSC, Victoria, BC, V8W 3V6, Canada. (nathan.gillett@ec.gc.ca; jiangnan.li@ec.gc.ca)

M. J. Iacono and E. Mlawer, Atmospheric and Environmental Research, Ltd., 131 Hartwell Ave., Lexington, MA 02421, USA. (miacono@aer.com; emlawer@aer.com)

A. I. Jonsson and M. Sigmond, Atmospheric Physics Group, Department of Physics, University of Toronto, 60 St. George St., Toronto, ON M5S 1A7, Canada. (andreas@atmosp.physics.utoronto.ca; sigmond@atmosp.physics.utoronto.ca)

A. Karpechko, Arctic Research Centre, Finnish Meteorological Institute, Täteläntie 62, FI-99600 Sodankylä, Finland. (alexey.karpechko@fmi.fi)

U. Langematz and S. Oberländer, Institut für Meteorologie, Freie Universität Berlin, Carl-Heinrich-Becker-Weg 6-10, D-12165 Berlin, Germany. (ulrike.langematz@met.fu-berlin.de; sophie.oberlander@met.fu-berlin.de)

P. Lemennais, Service d'Aeronomie du CNRS, 4 place Jussieu, F-75252 Paris CEDEX 05, France. (perrine.lemennais@aero.jussieu.fr)

B. Mayer, Lehrstuhl fuer Experimentelle Meteorologie, Ludwig-Maximilians-Universität, Theresienstrasse 37, 80333 München, Germany. (bernhard.mayer@lmu.de)

O. Morgenstern, National Institute of Water and Atmospheric Research, Private Bag 50061, Lauder, New Zealand. (o.morgenstern@niwa.co.nz)

G. Myhre, Center for International Climate and Environmental Research–Oslo, N-0318 Oslo, Norway. (gunnar.myhre@cicero.uio.no)

R. W. Portmann, Chemical Sciences Division, Earth System Research Laboratory National Oceanic and Atmospheric Administration, 325 Broadway, Boulder, CO 80305, USA. (robert.w.portmann@noaa.gov)

E. Rozanov, Physical-Meteorological Observatory/World Radiation Centre, CH-7260 Davos, Switzerland. (e.rozanov@pmodwrc.ch)

K. Shibata, Meteorological Research Institute, Tsukuba 305-0052, Japan. (kshibata@mri-jma.go.jp)